Clays and Clay Minerals, Vol. 57, No. 5, 616–637, 2009.

CLAYEY CAP-ROCK BEHAVIOR IN H_2O-CO_2 MEDIA AT LOW PRESSURE AND TEMPERATURE CONDITIONS: AN EXPERIMENTAL APPROACH

ERIC KOHLER[1], TEDDY PARRA[1], AND OLIVIER VIDAL[2]

[1] Institut Français du Pétrole, Direction Géologie-Géochimie-Géophysique, 1−4 Avenue de bois Préau, 92025 Rueil-Malmaison, France

[2] Laboratoire de Géodynamique des Chaînes Alpines, Université Joseph Fourier, 1381 rue de la piscine, BP 53, F-38041 Grenoble Cedex, France

Abstract—The storage of CO_2 in geological reservoirs requires an understanding of the impact of CO_2 on clay-rich sealing cap-rocks to identify and explore critical parameters that modify petrophysical properties such as permeability and fracturing. The purpose of this study was to investigate the effect of heating, under different hydrated-CO_2 partial pressures, on the chemical compositions and relative amounts of mineral phases in the Saint Martin de Bossenay (SMB, Paris Basin, France) cap-rock in order to identify possible mineral-phase transitions and to estimate reaction kinetics induced by the presence of excess dissolved CO_2.

X-ray diffraction, transmission electron microscopy, and electron microprobe analyses were employed to study mineral alteration, with particular attention given to visualization and quantification of the mineral evolution of clay minerals. In all the altered mixtures investigated, the illitization of clays was combined with the formation of anhydrite. These changes were accompanied by a dolomitization and a slight increase in the quartz content. The CO_2-rich samples crystallized Fe^{2+}-and K^+-enriched illites, whereas the CO_2-free experiments precipitated Al^{3+}-deprived and Mg^{2+}-enriched illites. Advanced characterizations of cap-rock material allowed reaction paths, induced by the increase in dissolved CO_2 in the porous media, to be determined precisely. The results place strong constraints on numerical models aimed at evaluating the safety of an SMB site.

Key Words—Cap-rock, Clays, CO_2 Storage, Experimental Alteration, Illite, Reactivity, Smectite.

INTRODUCTION

Greenhouse-gas sequestration in geological structures is a technical challenge which demands scientific case studies to assess the safety of the storage site. Many technical questions have to be answered such as CO_2 thermodynamics in brines, the trapping mechanisms in reservoir or deep aquifers, or the mechanical, petrophysical, and geochemical impact of CO_2 on geological structures and formations. In particular, these studies must answer the question of potential reactions between CO_2 or CO_2-rich brines and overlying cap-rocks.

Most of the studies in literature aimed at estimating and quantifying this reactivity were focused on numerical fluid−rock interaction models (Regnault *et al.*, 2005; Lagneau *et al.*, 2005; Andre *et al.*, 2007). In their approach, those authors were confronted by several difficulties because the integration of physico-chemical reactivity into predictive models requires precise knowledge of: (1) unstable mineral phases and what parameters control their reactivity; (2) their reaction rates; and (3) the transformation products. In the ideal case where all these parameters are well constrained, an attempt to answer these questions would enable validation of site choice, quantification of CO_2 storage capacity, and provide some confidence in any predictions of long-term safety. Knowledge of many thermodynamic data, solid-solution properties, and kinetic data for clay-rich materials has been lacking up to now. For these reasons but also because minerals such as clays have not been precisely characterized in terms of chemical composition, the reliability of any long-term predictions of cap-rock mineral reactivity and transformations using numerical models is very limited (Gaus *et al.*, 2005; Kaszuba *et al.* 2005).

In the present study, an experimental approach was chosen to: (1) characterize precisely the mineralogical assemblages and the chemical compositions of minerals before and after exposure to partial CO_2 pressure; (2) deduce a detailed reaction path describing the reactivity of the cap-rocks; and (3) establish the timing of the reaction fronts propagating through the matrix. Two types of experiments were conducted, which involved either powdered clay or cm-scale fragments, at constant pressure and temperature conditions, fixed duration, and various CO_2/H_2O and solid/fluid ratios. Because clay minerals exhibit very small sizes, complex interstratification, and may have a large range of compositions, different analytical techniques were combined (X-ray diffraction (XRD), electron microprobe analysis (EMPA), transmission electron microscopy (TEM)) to characterize and quantify the mineralogical

* E-mail address of corresponding author:
eric.kohler@ifp.fr
DOI: 10.1346/CCMN.2009.0570509

assemblages and to estimate the chemical composition of clays and carbonates, before and after alteration.

In a forthcoming study, the precise characterization of the samples before and after alteration will allow a numerical model to be built which will allow investigation of the influence of the different chemical and physical parameters on the evolution of the clayey matrix through time, and by numerical inversion of these results to estimate the kinetics of the propagation of the reaction fronts.

MATERIALS AND METHODS

Starting material

Brosse *et al.* (2006) identified an experimental site that would permit CO_2 injection in the Paris Basin (France), in a saline aquifer (Dogger). Experiments were conducted on natural clay from the Callovo-Oxfordian formation at St Martin de Bossenay (Bonijoly *et al.*, 2006), provided by Gaz de France (GdF), on cores of the SMB-18 well at 1560.95 m (SMB-18-1). The representativity of the sample was validated by the characterization of two other fragments at 1355.5 m (SMB-18-2) and 1677 m (SMB-18-3). The data allowed the assumption that the limited conservation technique did not prevent samples from cracking due to dehydration, bacterial alteration, and mineral oxidation. Apart from partial pyrite oxidation into gypsum, no evidence of large oxidation was observed, *i.e.* the gray-black color of the shale was unchanged.

All of the samples consist of quartz, calcite, dolomite associated with some Fe-rich calcite, and orthoclase, with some local occurrences of gypsum, pyrite, and a large amount of phyllosilicates: mixed-layer illite-smectite (I-S), muscovite, kaolinite, and chlorite. A detailed description of the mineralogy is presented in the results section below.

Experimental apparatus and conditions

The conditions used in the experiments (150ºC, 150 bar), and in particular the temperature conditions, are more extreme than those in the actual rocks (~70ºC, 100 bar), but allow for the shorter experimental time. From a thermodynamic point of view, many of the mineralogical changes due to the temperature shift are associated with dehydration. In this type of reaction, water is a by-product on the high-temperature side of the equilibrium, and any chemical change that decreases water activity would decrease the temperature of the transformation. As a consequence, the rock is likely to react with pore water during the CO_2 dissolution, as observed during thermal heating.

Two types of experiments were conducted using either powdered samples or cm-scale fragments at constant pressure and temperature, fixed duration, and different CO_2/H_2O ratios. The first set of experiments involved powdered samples in order to enhance reactivity by increasing exposed surface areas for interaction between fluids and minerals surfaces. The experiments were designed to determine precisely the reaction paths under different experimental conditions, and involved different proportions of H_2O and CO_2 to illustrate the impact of CO_2 fugacity on the reaction paths. The solid/solution ratios were also changed to differentiate the dissolution processes with small solid/solution ratios from precipitation processes with large solid/solution ratios. In the large solid/solution-ratio experiments, aqueous solutions were saturated more rapidly, promoting crystal germination and growth. The minerals precipitated were not necessarily the end-products but may have represented the first stages of solid-aqueous solution reactivity. However, the small amount of solution prevented any significant number of intermediate phases from precipitating from the system (Verlaguet *et al.*, 2006), so a small amount of equilibrium mineralogical assemblage was expected.

500 mg and 100 mg of powder sieved to 20 μm was enclosed in large-volume gold capsules (~10 cm long and 1 cm wide) with ~50 or 100 mg of CO_2, and 100 μL of deionized water (Table 1). CO_2 was added in solid state (−78ºC) in an N_2 glove box just before cold

Table 1. Experimental conditions for the runs conducted at 150ºC and 150 bar.

Experiment name	Duration (days)	Samples (mg)	Type of run (powder/ fragments)	Solution (μL)	Solid/ solution	Solution chemistry	CO_2 content
CO2-005	60	99	powder	100	1	deionized	0 mg
CO2-007	60	101	powder	100	1	deionized	68 mg
CO2-009	60	102	powder	100	1	deionized	99 mg
CO2-014	60	500	powder	100	5	deionized	0 mg
CO2-016	60	503	powder	100	5	deionized	66 mg
CO2-018	60	507	powder	100	5	deionized	112 mg
C3-030705-150-150-1 SMB-18-1-1	30	2225	fragment	10100	0.22	deionized	0 mg
C3-030705-150-150-1 SMB-18-1-2	30	2000	fragment	0	very small*	Water-saturated matrix	35 bar at 25ºC

https://doi.org/10.1346/CCMN.2009.0570509 Published online by Cambridge University Press

welding (Telsonic) at room temperature. As a reference, a CO_2-free mix was prepared. All experiments were conducted in pressure vessels placed within a furnace at the desired temperature (Béhar *et al.*, 1997). The temperature was measured using a chromel-alumel thermocouple placed inside the vessels and the pressure was monitored using a gauge with a N_2 gas medium. The cumulative uncertainties due to measurement and regulation were estimated to be within ±1% and ±1σ (2ºC: standard deviation on monitored temperature) for temperature and ±1% and ±1σ (5 bar: standard deviation on monitored pressure) for pressure. At the end of the experiment, the autoclaves were removed from the furnace, still under pressure, and cooled down in water. The autoclaves were then depressurized, and the products removed from the gold capsule and dried at room temperature. The second set of experiments used cm-scale fragments in an H_2O-medium or CO_2-medium with H_2O-saturated samples. The experiments made it possible to visualize and quantify approximately the progression of the reactive fronts through time. The experiments were conducted on externally heated PAAR® autoclaves (30 mL) with gold overlay placed in a furnace (Al Darouich *et al.*, 2006). The temperature was monitored using a chromel-alumel thermocouple placed inside the vessels and pressure was recorded continuously using a strain gauge. The cumulative uncertainties due to measurement and regulation were estimated to be within ±1% and ±1σ (2ºC: standard deviation on monitored temperature) for temperature and ±1% and ±1σ (5 bar: standard deviation on monitored pressure) for pressure. The uncertainties were obtained by measurements with a pressure- and temperature-calibrated sensor. About 2 g of cap-rock fragments was enclosed with ~10 mL of solid CO_2 or deionized water. Pressure was achieved by injection of N_2 after vacuum. For the pure-water experiment, the autoclave was put under vacuum before injection of N_2. In the CO_2 experiment, the autoclave was filled under atmospheric pressure in order to avoid water desaturation of the starting product. In this experiment, a maximum of 20 mL of air at atmospheric pressure was enclosed in the autoclave, which corresponds to an oxygen partial pressure of <0.2% of the total pressure at the running conditions (150ºC, 150 bar).

Analytical methods

Bulk-rock chemical and XRD analyses were conducted in order to investigate sediment heterogeneities and to select a representative fragment.

All experimental products were characterized by XRD. The powdered samples corresponding to CO_2-medium and CO_2-free experiments were analyzed using a Transmission Electron Microscope (EDS-AEM/TEM) standardized on synthetic clays for Si^{4+}, Al^{3+}, Ca^{2+}, and K^+. Some areas of the cm-scale fragment experiments were mapped using EMPA.

Bulk-rock analyses

Whole-rock geochemical analyses were carried out at the Centre Science des Processus Industriels et Naturels, Ecole Nationale Supérieure des Mines de St Etienne, France, by conventional X-ray fluorescence (XRF) and plasma optical emission spectrometry (ICP-OES). The XRF analyses were performed using an SRS3400 spectrometer, with glass discs/pressed pellets for major/trace elements, respectively. The ICP-OES analyses were performed on a JI Activa sequential device using acid solutions prepared by HF digestion.

Coupling these techniques is effective in overcoming the main drawback of each, *i.e.* sensitivity for minor and trace elements by XRF (<0.1% and 10 ppm, respectively) and reproducibility by ICP-OES (5%).

XRD

The clay-enriched fractions were obtained after a series of chemical and mechanical treatments. After grinding, chemical cementing agents were removed by acetic acid at room temperature for a few hours. The organic matter was oxidized by treating the carbonate-free sample with H_2O_2 at pH 9, maintained by NaOH, at 50ºC. After each chemical treatment, calcium from carbonates and products from organic matter oxidation were extracted in distilled water and solid particles were separated by centrifugation. The <2 μm fraction was extracted by sedimentation in distilled water. The clay-enriched fraction was Ca-exchanged with three repeated interactions of the powder in $CaCl_2$ solutions. The clay-enriched fractions had been mixed with molybdenum sulfur as an internal standard prior to XRD analysis.

The XRD patterns were collected using Cu$K\alpha_{1,2}$ radiation with a step size of 0.017º2θ and a counting time of 1.55 s per step, using a position-sensitive detector on an X'pertPro Panalytical diffractometer. In θ-θ configuration, XRD measurements were collected on oriented fractions on a glass plate at air-dried state, ethylene glycol-saturated state, and after heating to 350ºC for 3 h. The XRD patterns were decomposed with one or more components determined primarily by MLM2C calculations (Plançon and Drits, 2000) and which correspond to the I-S description of Lanson and Velde (1992).

The decomposition method was then combined with an inversion method which accounts for the chemical compositions of clays identified previously with MLM2C. The two first steps were followed by a series of interactions between inversion calculations and X-ray pattern decompositions of air-dried and ethylene glycol-saturated powders. The results were considered to be acceptable when statistical parameters obtained using *PeakFit*® (Systat Software Inc., Point Richmond, California) decomposition software were optimal with a minimum of I-S components. The whole-pattern fitting allowed the clays to be quantified (vol.%) and some chemical characteristics of the clays to be constrained.

https://doi.org/10.1346/CCMN.2009.0570509 Published online by Cambridge University Press

The XRD analyses in θ-2θ configuration were obtained using a parallel beam focused by an elliptic W/Si crystal mirror. The measurement was made on the clay-enriched fraction enclosed in a 1 mm glass capillary. Small variations in the intensities of the diffraction profile of the clay were detected using this technique which is not subject to difficulties with preferential orientation of particles.

Microprobe analyses

The electron microprobe analyses were conducted in order to map mineralogical assemblages and to determine the textural features of different minerals (De Andrade *et al.*, 2006). The EMP analyses were carried out using a Cameca SX100 microprobe. The analytical conditions used for the 'cartographic' mode were 15 kV accelerating voltage, probe current of 100 nA, 0.3 s for all elements, with a 1 μm spot size and a 5 μm step size. The analytical conditions used for the standardized analyses were 15 kV, 10 nA, 10 s for Si, Al, Fe, Mg, Ca, and S, and 15 s for Na and K. The electron microprobe was standardized on albite for Si and Na, alumina for Al, magnesium oxide for Mg, hematite for Fe, orthoclase for K, apatite for Ca, and zinc sulfide for S.

X-ray intensity maps of all elements were transformed to oxide wt.% concentration maps according to the procedure of De Andrade *et al.* (2006), using high-quality point analyses in the analytical conditions described previously. Statistical cluster analysis was used to identify the different phases occurring in the samples (see De Andrade *et al.*, 2006 for the detailed procedure). For clays and carbonates clusters, a structural formula was calculated for each pixel using an 11 oxygen basis and a 1 oxygen basis, respectively, and assuming all Fe to be divalent. The maps of structural formulae were then filtered to remove pixel analyses located at the limit between different homogeneous phases (mechanical mixing on contaminated analyses). In the particular case of I-S which showed large compositional variations, analyses with an oxide sum of <65 wt.% or >96 wt.% were discarded. The remaining structural formulae were filtered using the set of equations detailed by Vidal and Parra (2000), Parra *et al.* (2002), and Vidal (2001), aimed at removing I-S pixel analyses that are not a linear combination of muscovite, celadonite, pyrophyllite, and triocahedral micas. The constraints also allow contaminated analyses to be excluded (Vidal and Parra, 2000).

Transmission electron microscopy

The analytical/transmission electron microscopy (AEM/TEM) analyses were carried out using an energy dispersive spectrometer (EDS) combined with a Transmission Electron Microscope (JEOL 2000FX EDS-AEM/TEM 200 kV) at the CEA Cadarache Laboratory (LMTE) to determine the clay compositions of the particles. The EDS detector was a Si-Li (Oxford Instrument) device. The electron beam was set in convergent mode and the spot size was ~10 nm. The spectra were acquired for 1 min with a dead-time of <10% and a count number between 1000 and 2000. Analyses were standardized using the K-factor method on synthesized minerals with chemistry close to clay composition when possible: phlogopite $Mg_3(Si_3Al)O_{10}(OH)_2K$ for Mg, Si, and K; kaolinite $Al_2Si_2O_5(OH)_4$ for Al; augite $(Ca,Na)(Mg,Fe,Al,Ti)(Si,Al)_2O_6$ for Ca; and olivine $(Mg,Fe)_2SiO_4$ for Fe. The powders were dispersed in deionized water and disaggregated in an ultrasonic bath for 1 min. An aliquot of the aqueous dispersion was then allowed to dry in the laboratory atmosphere on a 200 mesh copper grid covered by a carbon layer. The calcium exchange made it possible to calculate structural formulae with Ca in the smectite interlayer space and without other potential smectite interlayer cations such as Mg^{2+}, H_3O^+, or Fe^{2+} (Grim, 1953). The structural formulae of the clays were calculated assuming all Fe as Fe^{2+}. About 50 analyses were made per sample and potential contamination was excluded using the same criteria as those detailed previously for the selection of EMP analyses (Vidal and Parra, 2000).

RESULTS

The clayey cap rock before alteration

The chemical bulk analyses of the three original samples were very similar (Table 2). Maximum variations were observed for silica and calcium, which reflect local variations in the quartz and calcite proportions. X-ray diffraction of sample SMB-18-1 (Figure 1a) revealed that the cap-rock before alteration contained quartz, calcite, dolomite, some Fe-rich calcite, orthoclase, some local gypsum and pyrite, and a large amount of phyllosilicates. Four main phyllosilicates were identified: I-S, muscovite, kaolinite, and chlorites.

Secondary electron imaging (Figure 2a) and the mineralogical map obtained after conversion of the element microprobe mappings and following the preceding procedure of De Andrade *et al.* (2006) (Figure 2b) revealed that the spatial distribution of the minerals was homogeneous at the micron scale. Calcite and quartz were distributed homogeneously all over the map and the clay cluster that includes I-S, kaolinite, and chlorite did not exhibit local spatial enrichment in any of the clays.

The XRD patterns of oriented preparations were modeled using three I-S components for the illitic part and a pure smectite component. The results revealed that the first two I-S had an R1 ordered structure with 70% and 80% illite layers, respectively, while the third I-S contained a highly ordered structure with 95% illite layers and with a potential R3 ordering (Figure 1b,c) and can be attributed to muscovite. The spatial distribution and size of muscovite on the mineralogical map may

https://doi.org/10.1346/CCMN.2009.0570509 Published online by Cambridge University Press

Table 2. Bulk chemical analysis of three samples of SMB cap-rock obtained by ICP-AES.

Wt.%*	SMB-18-1	SMB-18-2	SMB-18-3
LOI**	18.87	23.71	21.49
SiO_2	42.74	34.55	38.55
TiO_2	0.69	0.55	0.62
Al_2O_3	12.67	10.89	12.32
Fe_2O_3	4.59	3.72	3.75
MnO	0.02	0.02	0.02
MgO	1.87	2.12	2.09
CaO	14.13	20.49	17.79
K_2O	2.66	2.31	2.63
Na_2O	0.26	0.29	0.22
P_2O_5	0.06	0.07	0.09
Total	98.55	98.71	99.57
ppm	SMB-18-1	SMB-18-2	SMB-18-3
V	105	82	95
Cr	100	88	96
Ni	43	43	45
Cu	16	17	19
Zn	29	50	32
Ga	12	12	14
Rb	119	106	124
Sr	253	295	284
Y	23	23	25
Zr	162	116	125
Nb	14	10	11
Ba	248	232	251
La	42	43	38
Pb	14	12	14
Ce	58	36	51
Th	7	8	8
U	0	0	0

* wt.%: weight percent
** LOI : loss on ignition at 1000ºC

argue in favor of a detrital origin. A vermiculite component, described by Claret (2001) as a potential minor phase in the deeper Callovo-Oxfordian clay, was not found in the sample.

To quantify the relative amounts of the different clays in the initial sample, an inversion calculation method on XRD patterns was carried out using the structural formulae obtained directly by AEM/TEM and EMP. The chemical compositions were readjusted, as described previously, in order to obtain the smallest difference between the modeled and the experimental XRD patterns. In the inversion, a montmorillonite end-member with 0.17 a.p.f.u. of Ca (no Al^{3+} in the tetrahedral sites, no Fe^{3+} or Fe^{2+} in the octahedral sites) was considered for the smectite component. This assumption had little impact on the inversion calculations. A lognormal distribution of the number of layers per particle, between 2 and 14, without stacking defect, was used for the illite-richer I-S and with a mean defect-free distance containing five layers for the other two (Ergun, 1970). Kaolinite was supposed to be defect-free to fit the intensities and widths of major peaks. After optimization, the mixed-layer illite-smectite mineral component contained 0.5 a.p.f.u. for Al in the tetrahedral site, 0.1 a.p.f.u. for Fe^{2+} and 0.2 a.p.f.u. for Mg^{2+} in the octahedral site, and 0.7 a.p.f.u. for K^+ in the interlayer space. Chlorites had a large Fe^{2+}/Mg^{2+} ratio, close to 0.67.

The optimization also gives the volume ratios of clay components which confirm that the interstratified illite-smectite minerals (70−95% of illite layers) are the most abundant (up to 75 vol.%). Among the I-S, the most abundant are clearly those with 85% of illite layers. The amount of Fe-chlorite was estimated to be ~11% and the amounts of kaolinite and micas were both close to 7% (Figure 1b, Table 3).

The bulk-rock composition of the initial sample (Table 5) was estimated from the abundance of the minerals obtained by surface counting on mineralogical maps (Table 3), and from the chemical compositions obtained with the microprobe and presented thereafter. The results showed a clear similarity with the bulk

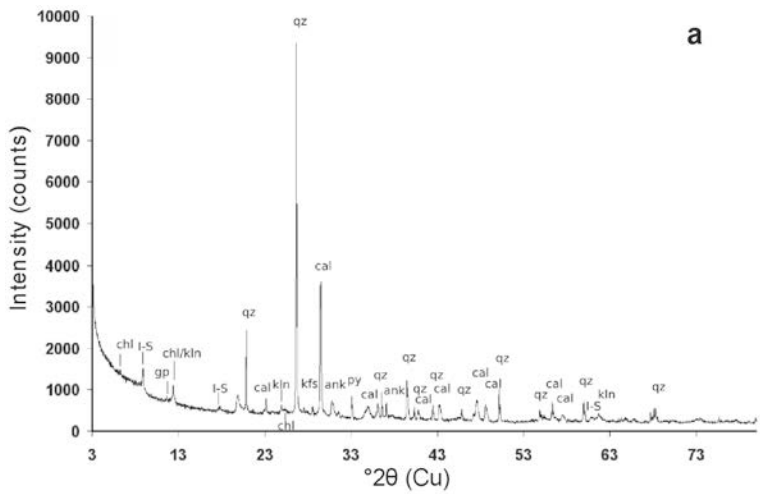

Figure 1 (*this and following page*). (a) XRD pattern, in reflection mode, of the bulk-rock sample SMB-18-1.

https://doi.org/10.1346/CCMN.2009.0570509 Published online by Cambridge University Press

chemical analyses (Table 2), except for Mg^{2+} and Ca^{2+}. The two differences are easily reduced by adjusting the calcite/dolomite ratio. The discrepancies support the suggestion that statistical cluster analysis overestimates the dolomite content slightly, probably by incorporating some of the dolomite compositions into the calcite cluster.

In the clay cluster, no chlorite or kaolinite analysis could be identified that precluded any estimate of the chemical composition of chlorite.

The EMP analyses were reported with the EDS results (Figure 3), in an R^{2+}-M^{+}-4Si ternary diagram (Velde, 1985; Meunier and Velde, 1989). The diagram revealed the octahedral occupancy (R^{2+}, sum of the octahedral divalent cations), the interlayer charge (M^{+}, sum of the interlayer cations multiplied by their valence), and the tetrahedral substitution (4Si, the number of tetrahedral silica cations for one site divided by 4) variations. The microprobe analyses cover a large area in the ternary plot, reflecting the fact that the numerical criteria cannot discard analyses contaminated by <2% of other particles such as quartz. The similarities in the EDS and WDS results are, however, satisfactorily close.

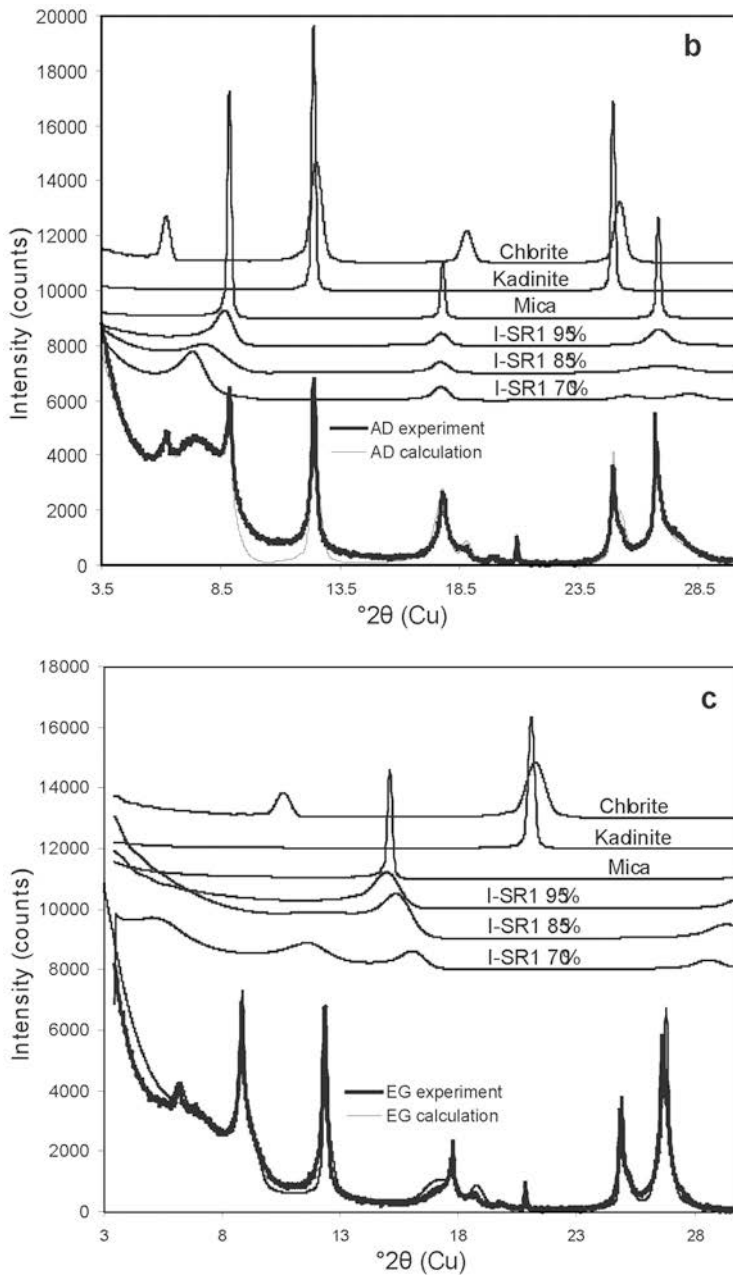

Figure 1 (*contd*.). (b,c) Comparison of calculated and measured XRD patterns of air-dried (b) and ethylene glycol-solvated sample (c).

https://doi.org/10.1346/CCMN.2009.0570509 Published online by Cambridge University Press

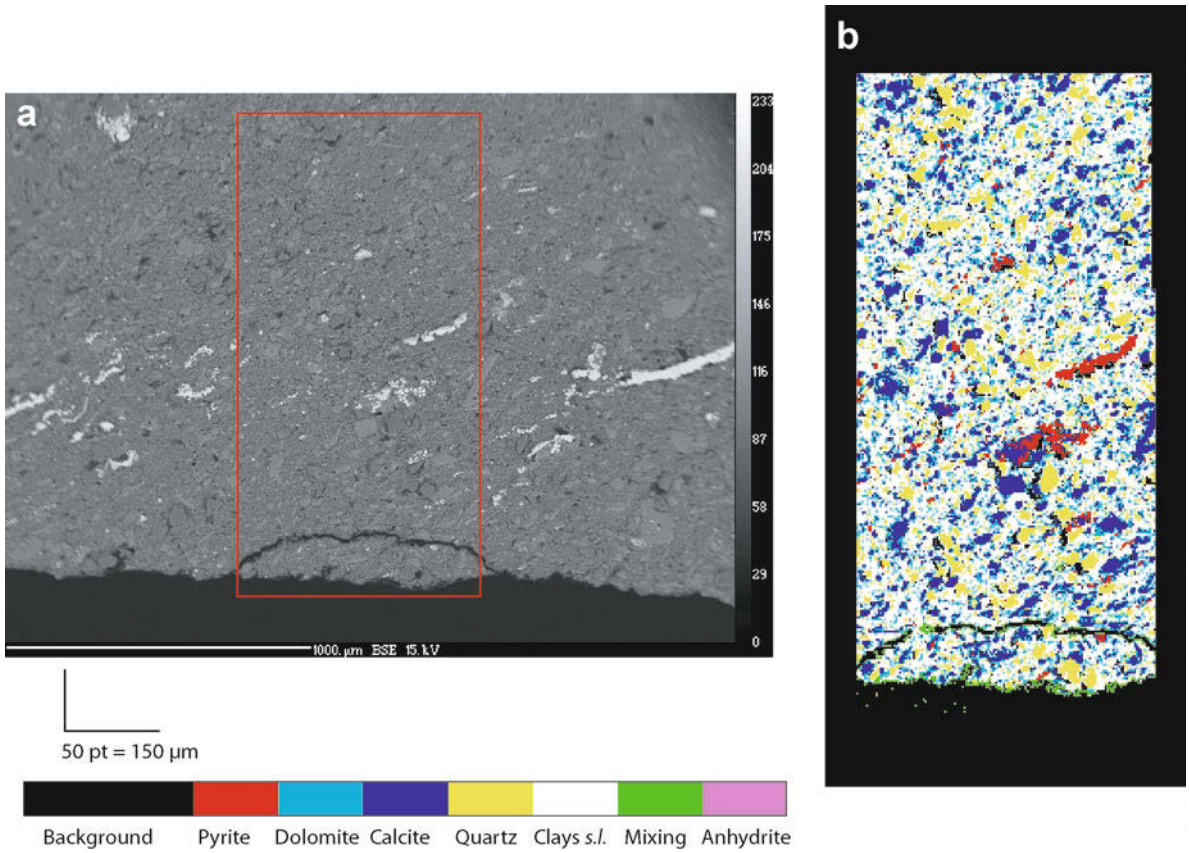

Figure 2. (a) Secondary electron imaging of initial sample; (b) minerals mapping of the initial sample.

The clays exhibited a large Si^{4+} content close to 3.6 a.p.f.u. while the Al^{3+} and K^{+} contents varied widely, from 1.7 to 2.4 a.p.f.u. and from ~0.2 to 0.7 a.p.f.u., respectively. The Mg^{2+} and Fe^{2+} contents were very close to the values obtained from the XRD inversion, ~0.1 and 0.2 a.p.f.u., respectively (Table 4).

Some of the I-S analyses may present an octahedral content of <2.00 a.p.f.u., as was noted by Ransom and

Table 3. Quantitative analysis of initial SMB cap-rock sample and after alterations.

Minerals	Analytical protocol	Vol.% before alteration	Vol.% after CO_2 alteration	Vol.% after water alteration
Clays	Microprobe mapping	40.1	50.0	42.8
Dolomite	Microprobe mapping	24.8	14.6	18.9
Calcite	Microprobe mapping	16.8	9.9	10.6
Quartz	Microprobe mapping	14.1	23.0	16.5
Pyrite/anhydrite	Microprobe mapping	4.2	2.5	11.2
Clays				
Illite-smectite minerals (70–95% of illite layer)	XRD on <2 µm oriented powder	75.1	87.8	86.5
Fe-chlorite	XRD on <2 µm oriented powder	11.0	3.0	5.5
Kaolinite	XRD on <2 µm oriented powder	7.0	6.8	3.5
Mica	XRD on <2 µm oriented powder	7.0	5.7	4.5
Calcite/Dolomite	Microprobe mapping	0.7	0.7	0.6
Clays/Quartz	Microprobe mapping	2.8	2.2	3.2
(Dolomite+Calcite)/ (Clays+Quartz)	Microprobe mapping	0.8	0.3	0.5

https://doi.org/10.1346/CCMN.2009.0570509 Published online by Cambridge University Press

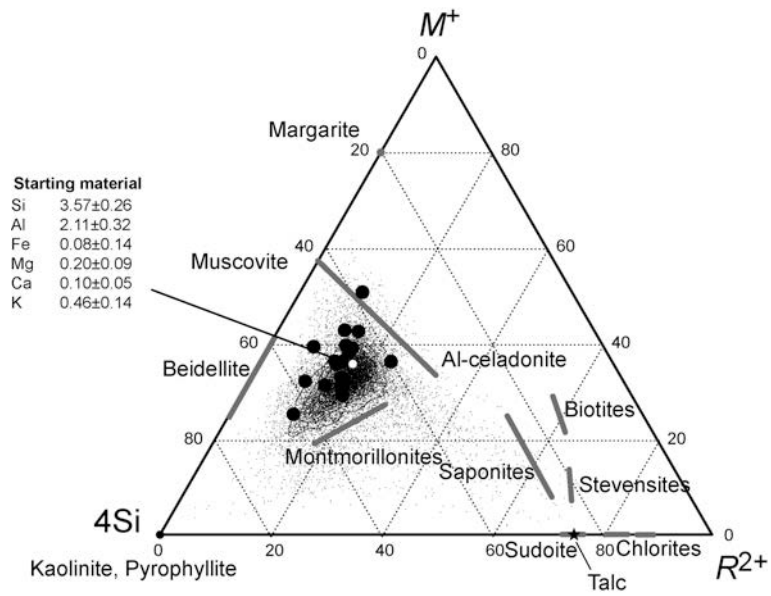

Figure 3. Comparison of EDS-TEM (black circles) and microprobe I-S analyses (black points) in an *MR*Si ternary diagram. White circle: mean of EMPA data.

Helgeson (1986) who attributed it to the illitic substitution [$(Fe^{2+}, Mg^{2+})K^{+} = Al^{3+VI}$] (Velde, 1985), which, combined with the di-trioctahedral substitution [$\square^{VI}Al^{3+VI}Al^{3+VI} = 3(Fe^{2+},Mg^{2+})^{VI}$] can lead to very small octahedral contents. The succession of substitutions may also explain the relatively large Si content that is normally attributed to high-pressure phengites (Meunier and Velde, 1989), but if associated with a very small (Fe^{2+}+Mg^{2+}) content is symptomatic of illite compositions. The large variations in clay compositions define a trend between a smectite-rich end-member characterized by a Ca^{2+} content between 0.20 and 0.32 and K^{+}-content between 0.10 and 0.38, and an illite end-member with a K^{+}-content close to unity (Figure 3, Table 4). This evolution of composition may be due to variations in the smectite percentage in the mixed-layered particles and/or to variations of the smectite and illite end-member compositions. In the latter case, the compositional variations may be explained by five substitutions (Velde, 1989; Parra *et al.*, 2002):

Fe^{2+} to Mg^{2+} substitution [$Fe^{2+VI} = Mg^{2+VI}$]
Tschermak substitution [$Si^{4+IV}(Mg^{2+},Fe^{2+})^{VI} = Al^{3+IV}Al^{3+VI}$]
pyrophyllitic substitution [$(Na^{+},K^{+})^{I}Al^{3+IV} = \square^{I}Si^{4+IV}$]
di/trioctahedral substitution [$\square^{VI}Al^{3+VI}Al^{3+VI} = 3(Fe^{2+},Mg^{2+})^{VI}$]
illitic substitution [$(Fe^{2+}, Mg^{2+})K^{+} = Al^{3+VI}$]
calcium substitution [$Ca^{2+}Al^{3+} = Si^{4+}(Na^{+}, K^{+})$]

In the two processes, the evolution of compositions resulted from re-equilibration processes through time with some local recrystallizations of pre-existing minerals as observed in low-temperature metamorphic rocks (Parra *et al.*, 2005; Vidal *et al.*, 2005).

Powdered samples altered in H_2O-CO_2 media

In all experiments with and without CO_2, XRD analyses in transmission mode showed only an increase in the proportions of anhydrite. Using ZnO as an internal standard (Środoń *et al.*, 2001), some tiny variations in the proportions of quartz and carbonate may have occurred, depending on the initial fluid composition and rock/fluid proportions.

Water-medium experiment. No change in the proportions of carbonates or quartz were detected by XRD, though the pattern for experiment CO2-014 did reveal an illitization of the primary clays.

The EDS-AEM/TEM analyses (CO2-005) exhibited no change in the Fe^{2+} and Mg^{2+} contents of I-S, but evidence of a large increase in the Ca^{2+} content was observed, along with a significant decrease in the octahedral occupancy due to the decrease in the total Al^{3+} content (Table 6). As a result, some analyses plotted above the muscovite–celadonite binary (Figure 4a). In order to check for an eventual calcium substitution, the (Si^{4+}+K^{+}) *vs.* the (Al^{3+IV}+Ca^{2+}) content of clays before and after alteration was reported together with the domain of "classic" I-S, between margarite, pyrophyllite, and celadonite components (Figure 5). Half of the analyses of the rock sample after alteration plotted outside the domain and correspond to the Ca^{2+}-richer analyses. The analyses (Table 6) were related to a supposed total of interlayer cations of >1.00 a.p.f.u. and a sum of octahedral content of <1.8 a.p.f.u. The low octahedral occupancy observed by Ransom and Helgeson (1993), after a compilation of the compositional variations of natural illite and smectite, was never associated with either a large Ca^{2+} content, or

https://doi.org/10.1346/CCMN.2009.0570509 Published online by Cambridge University Press

Table 4. EDS/TEM analysis of the initial sample and structural formulae calculated on an 11 oxygen basis (n = 28).

Oxide wt.%	Filtered AEM/TEM analysis of the initial SMB sample																							
SiO_2	60.19	60.04	59.07	61.28	57.46	59.09	60.53	59.99	56.89	59.36	58.25	57.11	60.61	56.08	55.73	56.22	59.76	58.03	58.73	56.77	57.94	58.60	56.73	58.65	57.44
Al_2O_3	26.99	26.76	23.68	25.50	31.53	30.33	29.01	33.14	28.90	30.88	31.13	30.04	28.37	31.88	33.83	27.99	32.75	35.49	27.34	29.35	32.11	23.90	27.55	31.29	29.02
FeO	1.48	3.05	2.59	1.40	1.62	0.76	1.46	1.14	1.28	1.42	1.23	1.63	1.54	1.19	1.36	1.30	1.02	0.81	1.53	1.15	0.53	2.58	2.03	1.12	2.37
MgO	2.57	2.12	5.14	2.40	2.46	2.42	3.15	1.52	2.88	3.10	2.96	2.74	2.84	2.68	2.23	2.41	1.48	1.61	2.53	2.24	1.70	4.62	3.52	3.04	2.91
CaO	1.70	4.43	1.17	5.83	1.85	1.25	1.04	0.58	1.33	1.63	1.11	1.43	1.33	1.19	1.17	3.71	2.13	1.75	3.90	4.36	4.62	3.55	4.88	1.38	3.52
K_2O	7.08	3.60	8.36	3.58	5.09	6.15	4.82	3.62	8.72	3.61	5.33	7.06	5.30	6.99	5.69	8.37	2.86	2.32	5.97	6.13	3.10	6.75	5.30	4.52	4.74
Calculated structural formulae																									
Si^{IV}	3.69	3.67	3.68	3.73	3.49	3.59	3.65	3.57	3.53	3.56	3.53	3.51	3.67	3.44	3.39	3.52	3.56	3.45	3.61	3.50	3.49	3.65	3.51	3.54	3.52
Al^{IV}	0.31	0.33	0.32	0.27	0.51	0.41	0.35	0.43	0.47	0.44	0.47	0.49	0.33	0.56	0.61	0.48	0.44	0.55	0.39	0.50	0.51	0.35	0.49	0.46	0.48
Al^{VI}	1.64	1.59	1.42	1.55	1.75	1.75	1.71	1.90	1.65	1.75	1.75	1.69	1.69	1.75	1.82	1.58	1.86	1.93	1.59	1.64	1.77	1.40	1.52	1.76	1.62
Al tot	1.95	1.92	1.74	1.82	2.26	2.16	2.06	2.33	2.12	2.19	2.22	2.18	2.02	2.31	2.43	2.06	2.30	2.48	1.98	2.14	2.28	1.75	2.01	2.22	2.10
Fe	0.08	0.16	0.14	0.07	0.08	0.04	0.07	0.06	0.07	0.07	0.06	0.08	0.08	0.06	0.07	0.07	0.05	0.04	0.08	0.06	0.03	0.13	0.11	0.06	0.12
Mg	0.23	0.19	0.48	0.22	0.22	0.22	0.28	0.14	0.27	0.28	0.27	0.25	0.26	0.25	0.20	0.22	0.13	0.14	0.23	0.21	0.15	0.43	0.32	0.27	0.27
Ca	0.11	0.29	0.08	0.38	0.12	0.08	0.07	0.04	0.09	0.10	0.07	0.09	0.09	0.08	0.08	0.25	0.14	0.11	0.26	0.29	0.30	0.24	0.32	0.09	0.23
K	0.55	0.28	0.66	0.28	0.39	0.48	0.37	0.27	0.69	0.28	0.41	0.55	0.41	0.55	0.44	0.67	0.22	0.18	0.47	0.48	0.24	0.54	0.42	0.35	0.37
Σoct.	1.95	1.94	2.04	1.84	2.05	2.01	2.06	2.10	1.99	2.10	2.08	2.02	2.03	2.06	2.09	1.87	2.04	2.11	1.90	1.91	1.95	1.96	1.95	2.09	2.01
Σint.	0.66	0.57	0.74	0.66	0.51	0.56	0.44	0.31	0.78	0.38	0.48	0.64	0.50	0.63	0.52	0.92	0.36	0.29	0.73	0.77	0.54	0.78	0.74	0.44	0.60

Table 4 (*contd.*)

				Mean	Min	Max
SiO_2	59.79	57.43	59.01	58.46	55.73	61.28
Al_2O_3	24.90	33.48	28.77	29.50	23.68	35.49
FeO	1.84	1.37	1.53	1.51	0.53	3.05
MgO	3.63	2.12	2.76	2.71	1.48	5.14
CaO	3.01	1.13	1.99	2.39	0.58	5.83
K_2O	6.83	4.46	5.94	5.44	2.32	8.72
a.p.f.u.						
Si^{IV}	3.69	3.46	3.60	3.56	3.39	3.73
Al^{IV}	0.31	0.54	0.40	0.44	0.27	0.61
Al^{VI}	1.50	1.84	1.67	1.68	1.40	1.93
Al tot	1.81	2.38	2.07	2.12	1.74	2.48
Fe	0.10	0.07	0.08	0.08	0.03	0.16
Mg	0.33	0.19	0.25	0.25	0.13	0.48
Ca	0.20	0.07	0.13	0.16	0.04	0.38
K	0.54	0.34	0.46	0.42	0.18	0.69
Σoct.	1.93	2.10	2.00	2.01	1.84	2.11
Σint.	0.74	0.41	0.59	0.58	0.29	0.92

n: number of analyses; Σoct.: sum of octahedral cations (a.p.f.u.); Σint.: sum of interlayer cations (a.p.f.u.)
a.p.f.u. values are framed whenever Al total <2.15, Mg >0.25, K >0.48, or Fe >0.08.

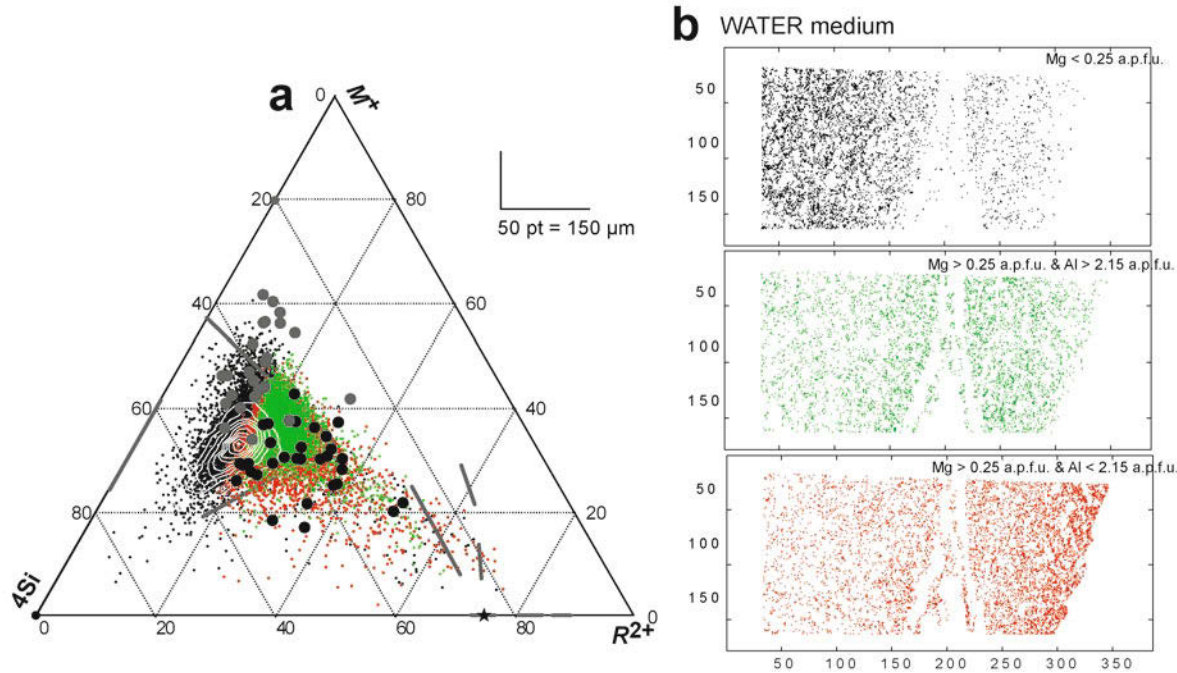

Figure 4. (a) Black circles: corrected EDS-TEM analyses of water-altered samples (see text for further explanations). Grey circles: EDS-TEM analyses of water-altered samples. (b) Maps of the filtered I-S EMPA.

with a sum of interlayer cations of >1 a.p.f.u.. From this observation, the octahedral Fe^{2+} and Mg^{2+} cations were probably exchanged by some Ca^{2+}. To correct this artifact, the Ca^{2+} content was limited to the Ca^{2+} content of the initial clays (0.15 a.p.f.u.), and the difference was added to the octahedral (Fe^{2+}+Mg^{2+}) sum, keeping the Fe^{2+}/Mg^{2+} ratio as a constant. The procedure led to the displacement of the analyses into the domain compatible

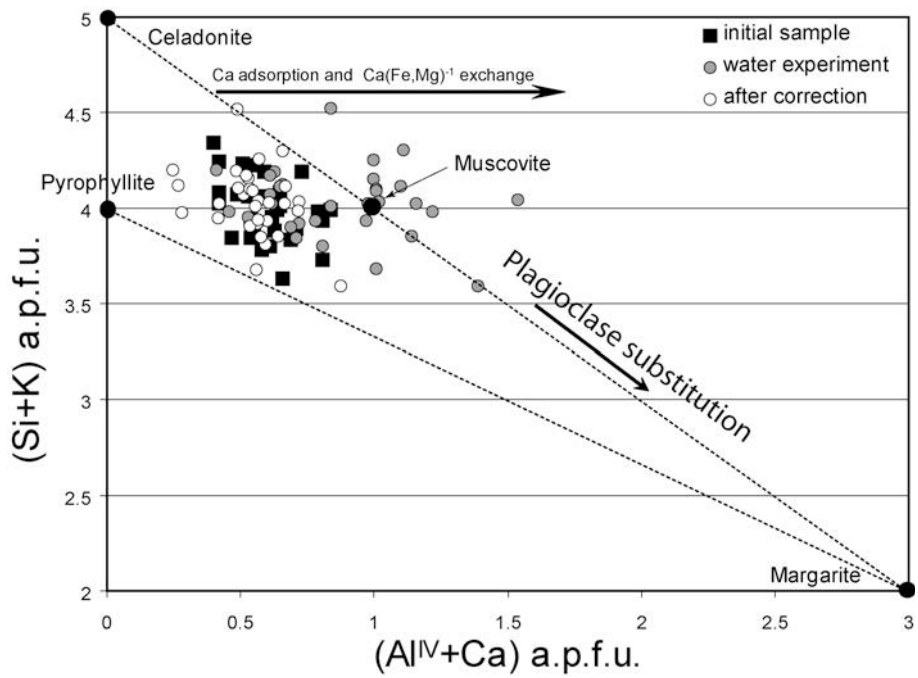

Figure 5. (Si+K) a.p.f.u. *vs*. (Al^{IV}+Ca) a.p.f.u. representing the plagioclase substitution: SiK $(Al^{IV}+Ca)^{-1}$. Grey circles: EDS-TEM analyses before correction. White circles: EDS-TEM analyses after correction (see text for further explanation).

https://doi.org/10.1346/CCMN.2009.0570509 Published online by Cambridge University Press

Table 5. Bulk-rock analyses recalculated from the chemical compositions of minerals obtained using the different analytical techniques (see text for more detail).

	Clays	Chlorite	Kaolinite	Muscovite	Dolomite	Calcite	Quartz	Pyrite			
Vol.%	30.1	4.4	2.8	2.8	24.8	16.8	14.1	4.2		With pyrite	Without pyrite
Molar volume (cm^3/mol)	139.68	216	99.52	140.87	32.16	36.9	22.69	24.00		Wt.%	Wt.%
Si	3.57	3	2	3			1		SiO_2	43.3	46.2
Al	2.11	1	2	3					Al_2O_3	13.8	14.8
Fe	0.08	4			0.03	0.02		1/0	Fe_2O_3	11.2	5.1
Mg	0.20	1			0.55	0.08			MgO	9.7	10.3
Ca	0.10				0.42	0.9			CaO	19.4	20.8
K	0.46			1					K_2O	2.6	2.8

with the chemical composition of clays (Figure 5), and toward the celadonite end-member or the trioctahedral binary in the R^{2+}-M^{+}-4Si diagram. This trend was confirmed by the EMPA obtained on polished sections (not Ca^{2+}-exchanged) and detailed thereafter.

CO_2-H_2O experiments. The CO_2-H_2O experiments involved experiments CO2-007, CO2-009, CO2-016, and CO2-018 (Table 1). In the experiments with a large solution/solid ratio (CO2-016 and CO2-018), calcite and quartz remained constant but the proportions of Mg-enriched calcite and dolomite increased (21 and 40 vol.%, respectively). No evidence of variations in the proportions of clay was seen.

Experiments conducted with a small solution/solid ratio (CO2-007 and CO2-009) showed an illitization of the initial clays. On the interlayer distance (nm) *vs.* full width at half maximum (FWHM, º2θ Cu) diagram (Lanson and Velde, 1992), the results of XRD inversions of the oriented clay fractions were plotted (Figure 6). The FWHM decreased with increase in illite crystallite thickness, while *d* (nm), which corresponds to the 001 illite peak, moved toward 1 nm with the increase in the illitic content in the mixed-layered minerals. The initial sample was characterized by the three I-S components identified previously. In all experiments, the parameters vary according to illitization for all components. The 'smectite-enriched' I-S components were the most

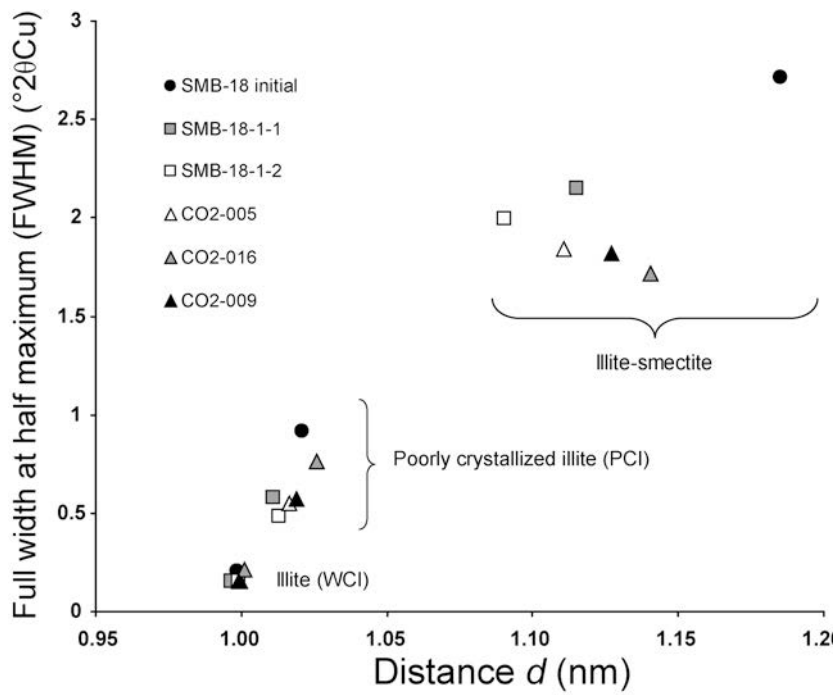

Figure 6. Full width at half maximum (FWHM) (º2θ) of the 001 peak *vs.* distance *d* (nm) between the layers of I-S particles, calculated from XRD patterns of air-dried oriented preparations. See Table 1 for a list of experimental conditions.

https://doi.org/10.1346/CCMN.2009.0570509 Published online by Cambridge University Press

Table 6. EDS/TEM analysis of CO2-005 sample and structural formulae calculated on an 11 oxygen basis: (n = 25).

Oxide wt.%	Filtered AEM/TEM analysis of the initial SMB sample																						
SiO_2	56.34	57.32	63.48	57.66	56.19	53.70	57.33	57.69	57.95	60.90	60.10	54.68	58.35	57.50	57.62	51.05	63.25	55.65	58.16	53.23	54.88	56.91	55.95	55.35	53.36
Al_2O_3	29.33	29.55	25.25	26.38	24.94	25.45	31.66	31.72	27.57	29.12	28.38	26.83	30.55	28.08	28.81	31.53	24.46	23.37	27.75	29.66	24.90	27.61	23.92	27.74	26.23
FeO	1.81	1.75	1.25	2.09	1.21	0.88	1.07	1.60	1.54	1.29	1.65	2.21	0.94	1.05	1.62	2.83	1.32	2.17	1.33	1.01	2.08	3.30	1.73	2.07	3.00
MgO	2.88	2.59	3.70	4.75	2.60	4.11	1.36	1.44	2.08	2.06	0.88	2.59	1.97	3.11	1.73	1.00	2.59	3.97	2.59	2.19	1.57	0.64	0.85	1.25	1.31
CaO	3.87	3.62	3.99	2.74	8.15	8.36	4.45	3.15	3.27	2.91	4.33	8.55	3.52	2.53	8.16	8.71	3.65	7.97	3.59	5.58	7.47	5.38	6.25	6.66	7.49
K_2O	5.77	5.17	2.34	6.38	6.92	7.50	4.14	4.40	7.58	3.72	4.66	5.15	4.66	7.74	2.05	4.87	4.74	6.87	6.59	8.33	9.10	6.16	11.30	6.93	8.62
Calculated structural formulae																									
Si^{IV}	3.48	3.52	3.80	3.57	3.54	3.41	3.48	3.50	3.59	3.66	3.66	3.44	3.54	3.56	3.52	3.20	3.83	3.53	3.59	3.36	3.51	3.52	3.59	3.47	3.41
Al^{IV}	0.52	0.48	0.20	0.43	0.46	0.59	0.52	0.50	0.41	0.34	0.34	0.56	0.46	0.44	0.48	0.80	0.17	0.47	0.41	0.64	0.49	0.48	0.41	0.53	0.59
Al^{VI}	1.61	1.65	1.58	1.49	1.40	1.32	1.75	1.77	1.61	1.73	1.70	1.43	1.73	1.60	1.59	1.53	1.58	1.28	1.60	1.57	1.39	1.53	1.40	1.52	1.38
Al tot	2.13	2.13	1.78	1.92	1.86	1.91	2.27	2.27	2.02	2.07	2.04	1.99	2.19	2.04	2.07	2.33	1.75	1.75	2.01	2.21	1.88	2.01	1.81	2.05	1.97
Fe	0.09	0.09	0.06	0.11	0.06	0.05	0.05	0.08	0.08	0.06	0.08	0.12	0.05	0.05	0.08	0.05	0.07	0.12	0.07	0.05	0.08	0.03	0.05	0.07	0.07
Mg	0.27	0.24	0.33	0.44	0.24	0.39	0.12	0.13	0.19	0.18	0.08	0.24	0.18	0.29	0.16	0.27	0.23	0.38	0.24	0.21	0.20	0.30	0.17	0.19	0.29
Ca	0.26	0.24	0.26	0.18	0.55	0.57	0.29	0.21	0.22	0.19	0.28	0.58	0.23	0.17	0.53	0.59	0.24	0.54	0.24	0.38	0.51	0.36	0.43	0.45	0.51
K	0.45	0.40	0.18	0.50	0.56	0.61	0.32	0.34	0.60	0.29	0.36	0.41	0.36	0.61	0.16	0.39	0.37	0.56	0.52	0.67	0.74	0.49	0.93	0.55	0.70
Σoct.	1.97	1.98	1.97	2.04	1.70	1.76	1.92	1.98	1.88	1.97	1.86	1.79	1.96	1.94	1.83	1.85	1.88	1.78	1.91	1.83	1.67	1.86	1.62	1.78	1.74
Σint.	0.71	0.64	0.44	0.68	1.11	1.18	0.61	0.55	0.82	0.48	0.64	0.99	0.59	0.78	0.69	0.90	0.61	1.10	0.76	1.05	1.10	0.80	1.10	0.90	1.00

Table 6 (*contd.*)

	Mean	Min	Max
SiO_2	57.17	51.05	63.48
Al_2O_3	27.41	21.95	31.72
FeO	1.75	0.88	3.30
MgO	2.24	0.64	4.75
CaO	5.44	2.53	8.71
K_2O	5.98	2.05	11.30
a.p.f.u.			
Si^{IV}	3.54	3.20	3.83
Al^{IV}	0.46	0.17	0.80
Al^{VI}	1.54	1.28	1.77
Al tot	2.00	1.59	2.33
Fe	0.07	0.03	0.13
Mg	0.24	0.08	0.44
Ca	0.36	0.17	0.59
K	0.48	0.16	0.93
Σoct.	1.86	1.62	2.04
Σint.	0.81	0.44	1.18

n: number of analyses; Σoct.: sum of octahedral cations (a.p.f.u.); Σint.: sum of interlayer cations (a.p.f.u.)
a.p.f.u. values are framed whenever Al total <2.15, Mg >0.25, K >0.48, or Fe >0.08.

affected by the presence of CO_2 and revealed the greatest rate of illitization.

For the CO2-009 experiment, which was considered as the 'CO_2-enriched' fluid-rock mixture (Figure 7a), 50 EDS-AEM/TEM analyses were replicated in order to obtain representative compositions of the clays after alteration. An evolution of the chemical compositions of clays toward muscovite, which was accompanied by an increase in their maximum K content (see mean and maximum contents in Table 7) and an increase in the range of variations of the sum of the interlayer content (between 0.15 and 1.09 a.p.f.u.) was observed. The mean Ca^{2+}, Fe^{2+}, Mg^{2+}, Si^{4+}, and Al^{3+} contents in the clays before and after alteration were very similar.

Fragment samples altered in H_2O-CO_2 media

In both CO_2-medium and water-medium experiments, XRD of bulk samples and the results from oriented clay deposits show a clear illitization of the clays (Figure 6). The evolution was more pronounced in the CO_2-bearing experiments, and in the smectite-richer I-S component of both experiments.

The element microprobe mappings of the CO_2-bearing and water-medium experiments were converted to mineralogical maps (Figure 8). Only small areas of the rims of the polished fragments could be investigated by electron microprobe, so the CO_2 or the water medium is located to the right of the maps. In this case, local disequilibria due to diffusion of the medium through the pore space should induce chemical compositional changes in both the clays and carbonates on the rim and should propagate the reactive front from right to left on the analyzed area from the rim to the core of the sample.

In both experiments, gypsum crystallized on contact with pyrites at the rim and in cracks of the samples (Figure 8). The proportions of the minerals (Table 3), evaluated by surface counting of the groups determined from the pixel clustering of the compositional map, indicated an increase in the proportions of quartz in the CO_2 experiment and a small decrease in the H_2O experiments (Table 3). In both experiments, the carbonate contents tended to decrease, but this was more pronounced in the CO_2 experiment. In the water experiment, the dolomite/calcite ratio increased. In a Ca^{2+}-Fe^{2+}-Mg^{2+} ternary plot (Figure 9), an increase in the Mg content of calcite and dolomite in both experiments was observed. In the CO_2-bearing experiment (red dots), the increase in the Mg content of dolomite was even more significant and was combined with a decrease in the Fe content of both the calcite and dolomite. In the clays cluster, the proportions of I-S increased in both media, but in the CO_2 medium the increase was achieved at the expense of the Fe chlorite, while in the water medium the reaction may be attributed to the dissolution of kaolinite, chlorite, and micas all together. The EMP analyses of the clay cluster showed an increase in Mg and a decrease in Al associated with water diffusion into the pore matrix (Figure 8), whereas in the CO_2-bearing experiment, the increases were for both the Fe and K contents. The Fe^{2+} and K^{+} gradients were also present in the core of the sample, at the contact with the fractures, as seen in the BSE images (Figure 8, uppermost), suggesting that, in contrast to the experi-

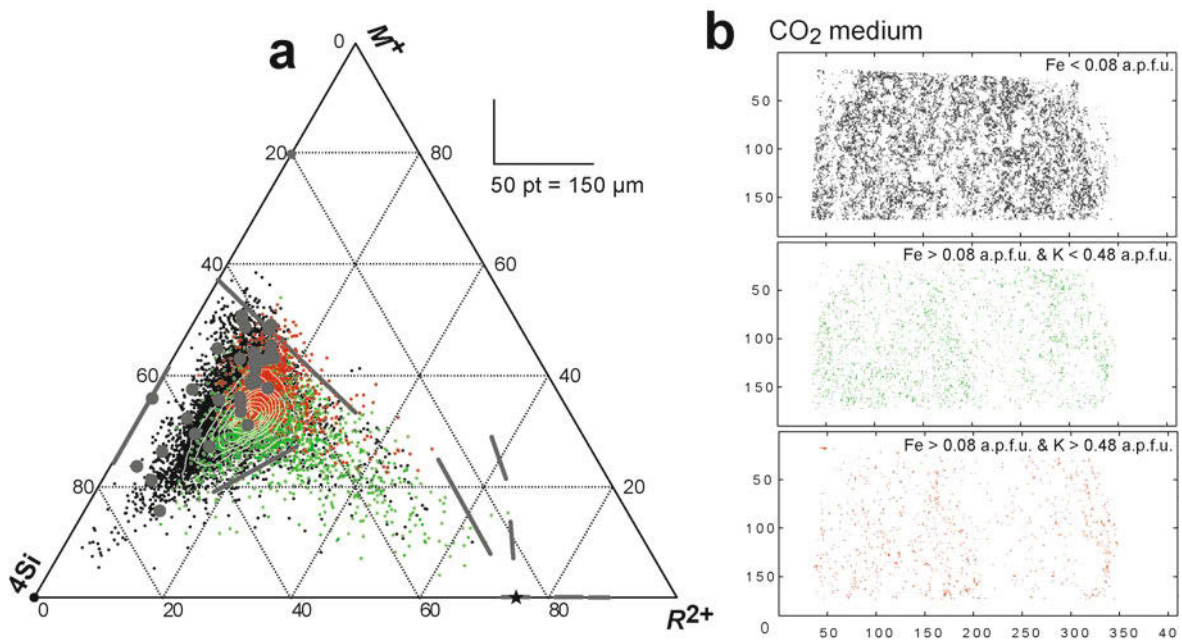

Figure 7. (a) Gray circles: EDS-TEM analyses of CO_2-altered sample. (b) Maps of the filtered I-S EMPA data.

https://doi.org/10.1346/CCMN.2009.0570509 Published online by Cambridge University Press

Table 7. EDS/TEM analysis of the sample CO2-009 and structural formulae calculated on an 11 oxygen basis: (n = 49).

Oxide wt.%	Filtered AEM/TEM analysis of the initial SMB sample																							
SiO_2	56.91	55.35	55.85	51.05	56.69	59.11	57.56	56.61	61.14	58.92	53.70	53.70	57.33	58.14	58.79	57.82	57.59	56.96	62.92	57.57	58.54	57.12	56.78	58.88	61.26
Al_2O_3	27.61	27.74	20.00	31.53	26.62	32.71	36.96	39.13	24.94	36.55	34.30	34.30	27.48	28.79	27.99	27.03	28.83	24.59	26.57	32.76	26.25	29.37	25.59	28.25	24.29
FeO	3.30	2.07	10.76	2.83	2.16	1.69	0.75	0.86	1.76	0.79	1.48	1.48	1.76	1.45	1.60	1.81	1.02	1.70	1.23	1.14	1.62	1.17	2.81	1.36	1.76
MgO	0.64	1.25	0.96	1.00	2.25	1.90	0.82	1.34	2.78	0.90	1.70	1.70	3.06	3.49	2.57	3.33	2.92	2.85	2.78	1.04	2.84	3.14	3.98	2.57	2.78
CaO	5.38	6.66	7.14	8.71	6.06	0.95	0.68	0.40	0.91	0.78	1.22	1.22	2.15	1.99	2.60	2.66	2.01	2.86	3.00	4.89	4.49	3.17	7.18	6.45	1.43
K_2O	6.16	6.93	5.29	4.87	6.22	3.65	3.23	1.65	8.47	2.07	7.60	7.60	8.22	6.14	6.45	7.35	7.63	11.04	3.49	2.61	6.26	6.01	3.66	2.49	8.47
Calculated structural formulae																									
Si^{IV}	3.52	3.47	3.51	3.20	3.53	3.54	3.42	3.34	3.77	3.47	3.32	3.32	3.57	3.56	3.61	3.58	3.55	3.62	3.77	3.47	3.62	3.51	3.53	3.57	3.79
Al^{IV}	0.48	0.53	0.49	0.80	0.47	0.46	0.58	0.66	0.23	0.53	0.68	0.68	0.43	0.44	0.39	0.42	0.45	0.38	0.23	0.53	0.38	0.49	0.47	0.43	0.21
Al^{VI}	1.53	1.52	0.99	1.53	1.48	1.85	2.01	2.06	1.58	2.01	1.82	1.82	1.58	1.64	1.64	1.56	1.65	1.46	1.65	1.80	1.53	1.64	1.40	1.60	1.55
Altot	2.01	2.05	1.48	2.33	1.95	2.31	2.59	2.72	1.81	2.54	2.50	2.50	2.01	2.08	2.03	1.98	2.10	1.84	1.88	2.33	1.91	2.13	1.87	2.03	1.76
Fe	0.03	0.07	0.05	0.05	0.07	0.08	0.04	0.04	0.09	0.04	0.08	0.08	0.09	0.07	0.08	0.09	0.05	0.09	0.06	0.06	0.08	0.06	0.15	0.07	0.09
Mg	0.30	0.19	1.01	0.27	0.28	0.17	0.07	0.12	0.26	0.08	0.16	0.16	0.28	0.32	0.24	0.31	0.27	0.27	0.25	0.09	0.26	0.29	0.37	0.23	0.26
Ca	0.49	0.55	0.42	0.39	0.50	0.06	0.04	0.03	0.06	0.05	0.08	0.08	0.14	0.13	0.17	0.18	0.13	0.19	0.19	0.32	0.30	0.21	0.48	0.42	0.09
K	0.36	0.45	0.48	0.59	0.41	0.28	0.24	0.12	0.67	0.16	0.60	0.60	0.65	0.48	0.51	0.58	0.60	0.90	0.27	0.20	0.49	0.47	0.29	0.19	0.67
Σoct.	1.86	1.78	2.05	1.85	1.83	2.10	2.12	2.22	1.93	2.13	2.06	2.06	1.95	2.03	1.96	1.96	1.97	1.82	1.96	1.95	1.87	1.99	1.92	1.90	1.90
Σint.	0.85	1.00	0.90	0.98	0.91	0.34	0.28	0.15	0.73	0.21	0.68	0.68	0.79	0.61	0.68	0.76	0.73	1.09	0.50	0.50	0.80	0.70	0.80	0.60	0.76
Oxide wt.%	Filtered AEM/TEM analysis of initial sample of SMB																							
SiO_2	58.65	61.59	57.00	59.64	53.95	61.64	56.30	55.77	55.17	58.50	59.68	57.50	57.41	54.84	53.80	56.87	53.57	54.09	65.14	63.77	57.21	57.46	58.69	58.45	
Al_2O_3	28.95	21.53	29.59	29.37	30.82	30.79	28.63	31.69	34.49	26.45	29.07	26.72	35.18	32.35	32.56	33.34	31.91	29.38	30.01	30.78	32.11	30.45	29.04	31.52	
FeO	1.63	2.03	0.96	1.76	1.34	1.32	1.06	1.09	0.46	1.86	1.90	2.60	0.33	0.39	0.46	1.29	1.69	1.84	0.37	0.18	0.94	1.28	1.76	0.93	
MgO	2.88	3.17	2.47	3.06	2.59	1.03	1.60	2.64	1.08	2.13	0.65	2.90	0.94	1.79	1.43	1.67	1.18	2.44	0.57	0.06	2.50	2.71	2.62	2.76	
CaO	2.54	2.52	1.76	1.22	2.99	1.76	2.05	2.40	1.46	2.39	3.36	2.62	1.80	2.20	1.23	0.75	0.85	0.97	0.30	2.60	1.13	1.54	2.30	1.59	
K_2O	5.34	9.16	8.22	4.95	8.31	3.47	10.37	6.40	7.35	8.67	5.33	7.66	4.35	8.43	10.52	6.08	10.80	11.27	3.61	2.61	6.11	6.55	5.60	4.75	
Calculated structural formulae																									
Si^{IV}	3.58	3.84	3.52	3.61	3.37	3.68	3.53	3.43	3.38	3.64	3.64	3.59	3.44	3.40	3.37	3.46	3.38	3.43	3.83	3.76	3.48	3.52	3.58	3.53	
Al^{IV}	0.42	0.16	0.48	0.39	0.63	0.32	0.47	0.57	0.62	0.36	0.36	0.41	0.56	0.60	0.63	0.54	0.62	0.57	0.17	0.24	0.52	0.48	0.42	0.47	
Al^{VI}	1.66	1.43	1.68	1.71	1.65	1.84	1.65	1.72	1.87	1.59	1.73	1.55	1.93	1.76	1.77	1.85	1.75	1.62	1.91	1.90	1.78	1.71	1.67	1.77	
Altot	2.08	1.59	2.16	2.10	2.28	2.16	2.12	2.29	2.49	1.95	2.09	1.96	2.49	2.36	2.40	2.39	2.37	2.19	2.08	2.14	2.30	2.19	2.09	2.24	
Fe	0.08	0.11	0.05	0.09	0.07	0.07	0.06	0.06	0.02	0.10	0.10	0.14	0.02	0.02	0.02	0.07	0.09	0.10	0.02	0.01	0.05	0.07	0.09	0.05	
Mg	0.26	0.29	0.23	0.28	0.24	0.09	0.15	0.24	0.10	0.20	0.06	0.27	0.08	0.17	0.13	0.15	0.11	0.23	0.05	0.01	0.23	0.25	0.24	0.25	
Ca	0.17	0.17	0.12	0.08	0.20	0.11	0.14	0.16	0.10	0.16	0.22	0.18	0.12	0.15	0.08	0.05	0.06	0.07	0.02	0.16	0.07	0.10	0.15	0.10	
K	0.42	0.73	0.65	0.38	0.66	0.26	0.83	0.50	0.57	0.69	0.41	0.61	0.33	0.67	0.84	0.47	0.87	0.91	0.27	0.20	0.47	0.51	0.44	0.37	
Σoct.	2.00	1.83	1.96	2.08	1.96	2.00	1.86	2.02	1.99	1.89	1.89	1.96	2.03	1.95	1.92	2.07	1.95	1.95	1.98	1.92	2.06	2.03	2.00	2.07	
Σint.	0.59	0.90	0.77	0.46	0.86	0.37	0.97	0.66	0.67	0.85	0.63	0.79	0.45	0.82	0.92	0.52	0.93	0.98	0.29	0.36	0.54	0.61	0.59	0.47	

Table 7 (*contd.*)

	Mean	Min	Max
SiO_2	57.61	51.05	65.14
Al_2O_3	29.73	20.00	39.13
FeO	1.63	0.18	10.76
MgO	2.07	0.06	3.98
CaO	2.64	0.30	8.71
K_2O	6.32	1.65	11.27
a.p.f.u.			
Si^{IV}	3.53	3.20	3.84
Al^{IV}	0.47	0.16	0.80
Al^{VI}	1.68	0.99	2.06
Al tot	2.15	1.48	2.72
Fe	0.07	0.01	0.15
Mg	0.22	0.01	1.01
Ca	0.18	0.02	0.55
K	0.50	0.12	0.91
Σ octa.	1.97	1.78	2.22
Σ int.	0.67	0.15	1.09

n: number of analyses
Σoct.: sum of octahedral cations (a.p.f.u.)
Σint.: sum of interlayer cations (a.p.f.u.)
a.p.f.u. values have been framed whenever K >0.48 and Fe >0.08.

ments conducted with powdered samples, the mineral reactivity in the fragments was mostly restricted to the zones of fluid percolation.

In order to differentiate the previous composition of the clays from those newly formed, two thresholds were defined for each experiment, depending on the observed evolutions of compositions. For the water-medium experiment, the different generations of clays were separated by setting the limit for alumina at <2.15 a.p.f.u. and the limit for Mg at >0.25 a.p.f.u.. For the CO_2-medium experiment, the limits were set at 0.48 and 0.08 a.p.f.u. for K and Fe, respectively. The Ca and Al contents were similar, before and after alterations.

By combining these thresholds, two generations of clays in each experiment could be differentiated. In the water-medium experiment, the formation of Al^{3+}-deprived and Mg^{2+}-enriched clays (Figure 4b, red dots map), which corresponds to chemical changes toward the trioctahedral phyllosilicate end-members (saponite series in Figure 4a), was observed close to the contact between the rim of the sample but also close to some fractures. Between the rim and the core clays, clay of a different composition was precipitated (Figure 4b, black dots map); the composition was close to the celadonite end-member (Figure 4a) with a Mg enrichment as the rim composition, but not yet impoverished in alumina (Figure 4b, green dots map) as the core composition. This generation of clays seems to be unstable as attested by their disappearance in the vicinity of the rim. The same type of compositional evolution was observed in the CO_2-medium experiments, where the formation of an Fe^{2+}- and K^+-rich generation of clays was observed at the rim of the sample, close to the phengite series, between the muscovite and the celadonite end-members (Figure 7a, red dots map). Between the rim and the core, some Fe^{2+}-rich and K^+-poor clays precipitated as precursors of the former corresponding to an evolution of the clays toward the beidellite series (Figure 7b, green dots map).

The distance between the core and the rim gives a good estimate of the kinetics of propagation of the reactive fronts during the 2 month duration of the experiments. In the case of the water-medium experiment, the reactions involving the clays penetrated the sample more deeply than in the CO_2-medium experiment. The unstable generation of clays penetrated the sample up to 500 and 200 μm in the water-medium and CO_2-medium experiments, respectively. They are seen on a restricted range of 300 and 150 μm, respectively, because they were replaced by the second generation of clays which appears to be less abundant and limited to the rims of the samples at distances of 200 and 100 μm in the water-medium and CO_2-medium experiments, respectively.

DISCUSSION

The location of the sampling corresponds to the most pronounced thermal gradient between Paris and Dijon (Velde and Vasseur, 1992). Complete characterization of the samples used in the experiments showed that the SMB formation experienced a high thermal gradient. The effect of the diagenesis was an illitization of the initial sediment and the formation of highly illitic I-S, as observed at the bottom of the Bure formation (ANDRA laboratory, France; Claret, 2001).

The EDS-AEM-TEM and microprobe results associated with decomposition of XRD results permitted estimation of bulk-rock compositions and the results were very close to those of bulk-rock analyses obtained using classical methods. The characterizations of samples using distinct I-S with different proportions of illite appeared to be somewhat arbitrary. In fact, the XRD patterns resulted from the sum of a large number of individual patterns corresponding to the heterogeneity of the clays included in the sample studied. In the present study, triple decomposition of clays with a well crystallized illite, a poorly crystallized illite, and an illite-smectite is insufficient to account for the chemical variabilities of the clays. The components may better represent three chemical and ordering end-members between which a continuous variation of clay chemical composition and their illite layer stacking may exist. The question that arises immediately when dealing with the chemical changes in clays relates to what the mechanisms are that allow them to re-equilibrate locally. The scale of re-equilibration depends on temperature and pressure, as explained by Vidal and Parra (2000). In

https://doi.org/10.1346/CCMN.2009.0570509 Published online by Cambridge University Press

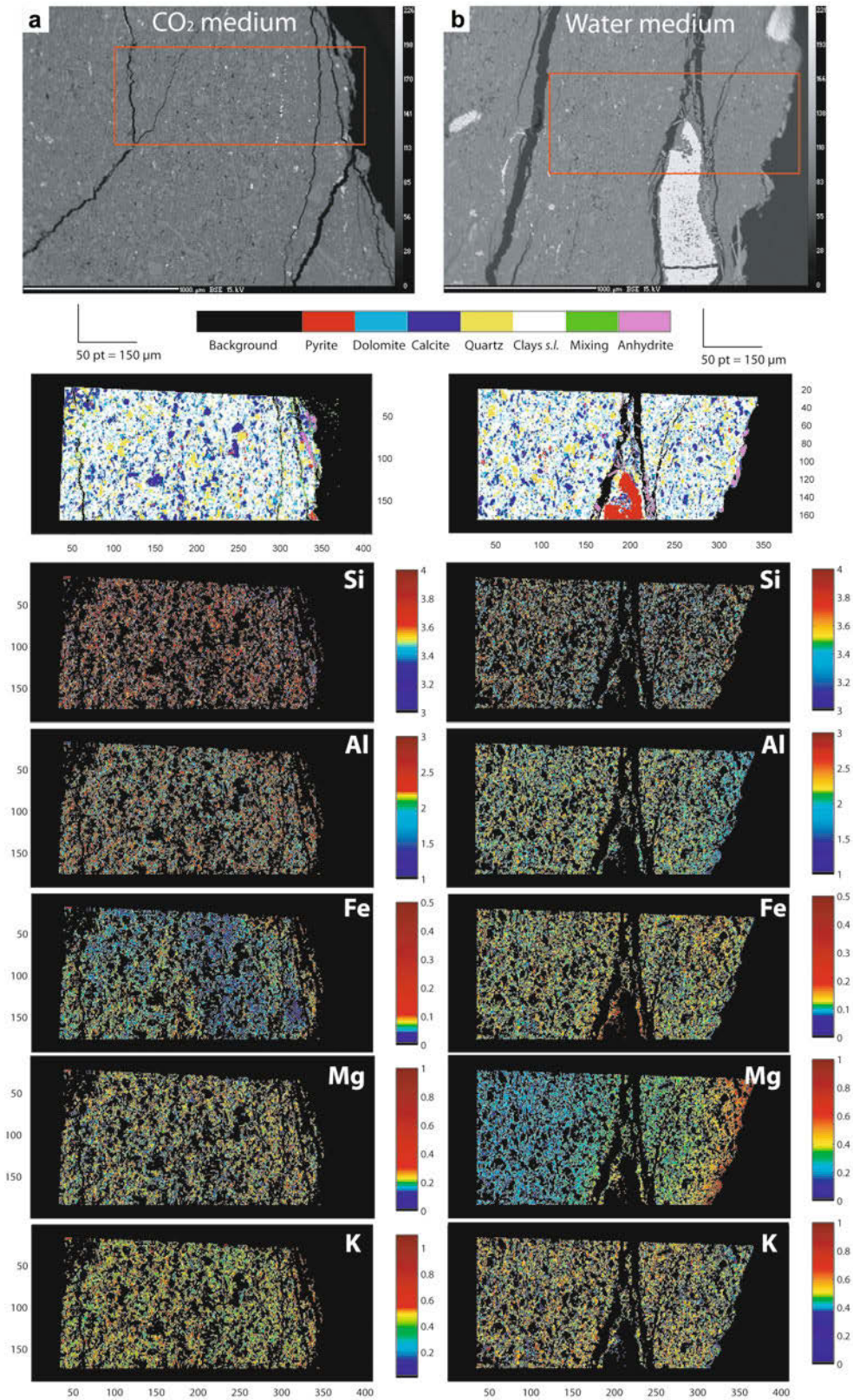

Figure 8. From top to bottom, secondary electron imaging, calculated mineralogical maps, and electron microprobe chemical mappings. (a): CO_2-altered sample; (b): water-altered sample.

https://doi.org/10.1346/CCMN.2009.0570509 Published online by Cambridge University Press

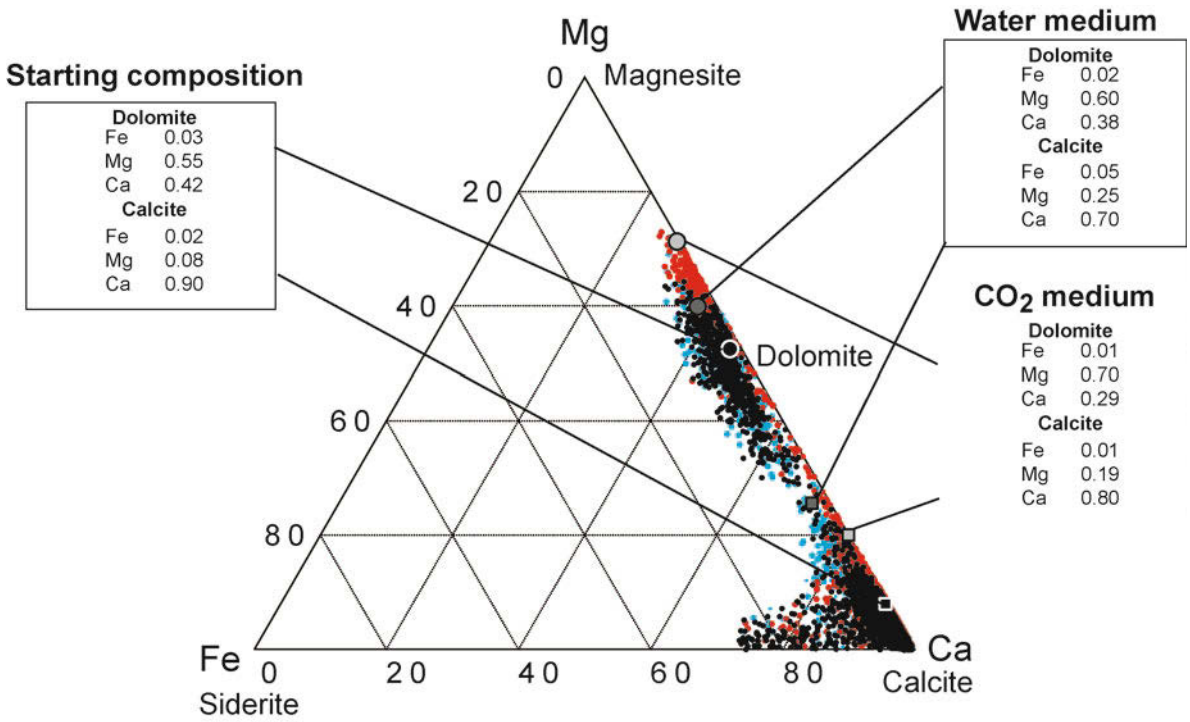

Figure 9. Colored dots correspond to EMP analyses of carbonates, before alteration (black), after CO_2 alteration (red), and after water alteration (blue). Circles and squares correspond to the means of dolomite and calcite compositions, respectively.

particular, the debate about the pressure-dissolution processes *vs.* the diffusion in the crystal still continues.

The EDS (TEM) and WDS (EMP) analyses of the three experimental fragments (before alteration, and after CO_2- and water-alterations) exhibited a total compatibility in terms of the types of clays (R^{2+}-M^{+}-4Si diagrams) and compositions (Tables 4, 6, 7).The standardization of EDS analyses gave rise to very good chemical analyses, compatible with the semi-quantitative EMP analyses, even though the spot sizes were different (a few tens of nm and 1 μm, respectively). The spot size of the electron probe did not induce significant errors, and the results were representative of the compositions of the clays in the different samples.

The I-S chemical variations, observed in the experiments, compared with the original sample may be associated either with a chemical change in smectite and illite layers or with a variation in the illite %. Determining the percentage of illite in individual I-S particles was impossible so no estimate of the role of each process was permitted. To illustrate the impact of the illite % variations on the composition of particles, different I-S compositions of particles corresponding to several illite % were plotted in an M^{+}-R^{2+}-4Si triangle (Figure 10a), using a constant composition for the smectite and illite end-members. The dissolution-reprecipitation processes were illustrated using a constant illite % set to 70%, as observed in the initial cap-rock sample, and different chemical variations of smectite and illite, keeping the interlayer charges constant (Figure 10b). The two ternary plots highlight the fact that, to account for the chemical changes in I-S, both phenomena must be implied, probably with some important variations in the interlayer charge. From a thermodynamic point of view, this chemical heterogeneity cannot be representative of stable assemblages, but rather is a result of the fluid-rock interactions and/or local re-equilibration during pressure-temperature variations, in distinct and more or less independent micro domains. This leads to the dissolution of unstable clays, and results in the precipitation of new ones.

In all experiments, the reactivity was surprisingly rapid. During an alteration time span of 2 months, a significant evolution of mineral proportions and compositions was observed on fragments and powders. However, a more significant reactivity was observed in fragment experiments than in the experiments involving powders. In fact, the opposite behavior would be expected because the powder experiments were thought to enhance reactivity. That behavior may potentially be explained by the existence of a gradient of thermodynamic chemical potentials, set by either the diffusion of CO_2 or water (dilution) media through the porous matrices.

To date, establishing an effect of CO_2/H_2O on solid/solution ratios has not been possible. This may be due to the short duration of the experiments.

https://doi.org/10.1346/CCMN.2009.0570509 Published online by Cambridge University Press

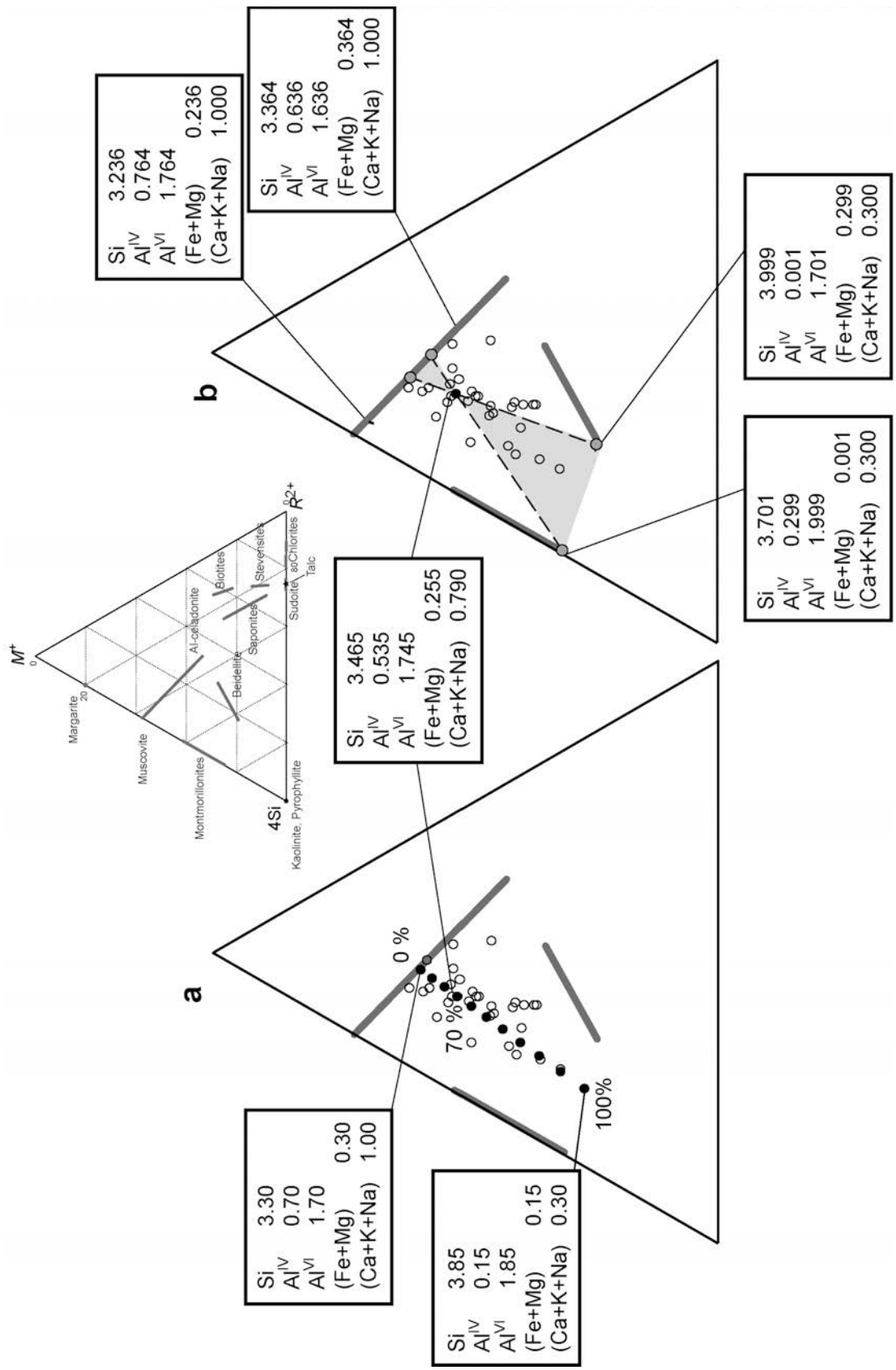

Figure 10. Calculated structural formulae plotted in *M*RSi ternary diagrams with (a) different illite% in I-S and fixed smectite and illite compositions; and (b) domain covered by the extreme compositions of smectites and illites for a fixed 70% illite content and a constant interlayer content.

https://doi.org/10.1346/CCMN.2009.0570509 Published online by Cambridge University Press

Water medium. In the water-medium experiment, a large amount of anhydrite growth and a clear decrease in the carbonates/silicates ratio were observed, resulting in an illitization of the I-S associated with an increase in the I-S content at the expense of Fe-chlorite and kaolinite. During these mineralogical changes, calcite and I-S were enriched significantly in Mg, while the alumina content of I-S was reduced (Figure 11).

In order to trace the reaction paths that allowed mineral end-products to crystallize, the different equilibria as a function of the starting mineral assemblages and the newly crystallized minerals were investigated. To account for the mineral composition changes, mean and extreme chemical compositions of I-S and carbonates obtained on microprobe mappings after alteration were used (Figures 9, 11).

With respect to the carbonates, two possible reactions (9 and 10) and one homogeneous equilibrium (8) were observed (note: reactions 1−7 were tests which produced no significant results, and therefore are not listed here):

$$3\text{Dol} + 0.3846\text{Cal} = 2.3846\text{Dol-W} + \text{Cal-W} \quad (8)$$

$$\text{Dol} + 0.0725\text{Py} + 1.8713\text{Cal} + 0.2538\text{O}_2 = 2.7988\text{Cal-W} + 0.0725\text{CO}_2 + 0.1450\text{Anh} \quad (9)$$

$$\text{Dol} + 0.0054\text{CO}_2 + 0.0107\text{Anhyd} = 0.8533\text{Dol-W} + 0.0054\text{Py} + 0.1520\text{Cal-W} + 0.0187\text{O}_2 \quad (10)$$

where Dol indicates dolomite, Cal indicates calcite, Py indicates pyrite, Anh indicates anhydrite and -W indicates a modifier of the mineral abbreviation in all equations where a given "mineral-W" signifies a mineral formed in water experiments. The abbreviations for rock-forming minerals used in this article are from Kretz (1983).

The two reactions cannot occur simultaneously but in chains, because reaction 10 needs some of the CO_2

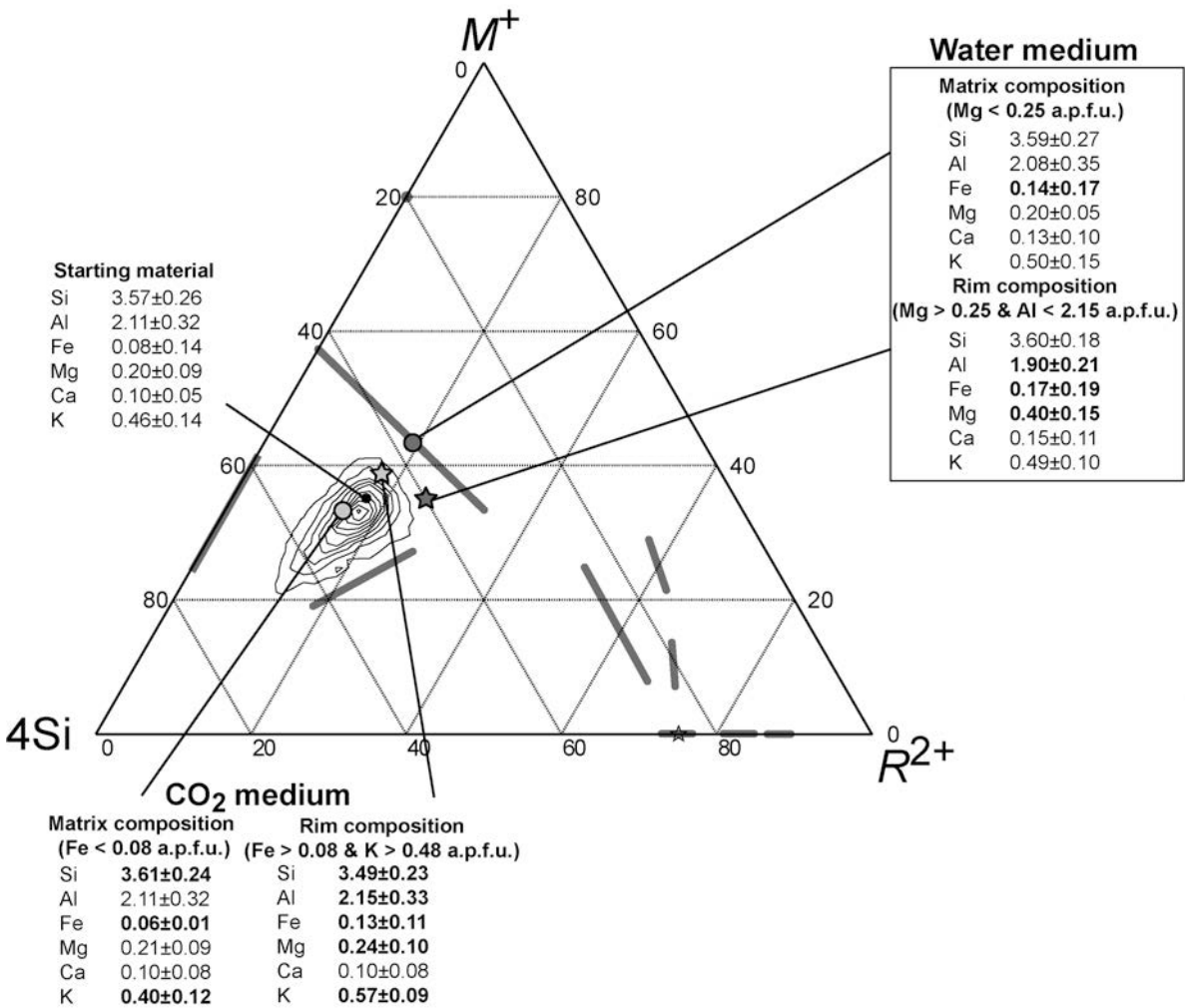

Figure 11. Mean structural formulae calculated on filtered EMP analyses as mentioned in the legend, highlighting the I-S chemical variations from core (circles) to rims (stars) of cm-scale fragments.

https://doi.org/10.1346/CCMN.2009.0570509 Published online by Cambridge University Press

produced by reaction 9. The two chain reactions imply an oxidation of pyrite to anhydrite (0.0725−0.0054) as observed in the experiments, a decrease in carbonate content, a consumption of O_2, and a production of CO_2. The model also implies an increase in the dolomite: calcite ratio. Involving Fe-chlorite and kaolinite in the possible reactants does not change the amount of calcite precipitated, even if some of the Fe in chlorites is allowed to be trivalent.

For the clays, only one reaction is possible and involves the secondary carbonates. The valence of the Fe in chlorites may decrease slightly the stoichiometric coefficients of reaction 11 concerning secondary clays, but does not change the reaction paths:

$$1.0652\text{clays} + 0.0167\text{Fe-Chl} + 0.1281\text{Qtz} + 0.3101\text{Dol-W} + 0.2491H_2O = 0.2470CO_2 + 0.0632\text{Cal-W} + 0.1905\text{Kln} + 0.0302\text{Anh} + \text{clays-W} \quad (11)$$

where Fe-Chl stands for chlorite, Qtz for quartz, and Kln for kaolinite.

In reaction 11, some anhydrite and calcite, from pyrite and dolomite, respectively, and a large amount of CO_2 and kaolinite were produced.

CO_2 medium. In the CO_2-medium experiment, an illitization of I-S together with an increase in quartz content was observed. The carbonates and chlorites were partially consumed, and a localized oxidation of pyrite to anhydrite was observed. Calcite and dolomite recrystallization were accompanied by an increase in their Fe and Mg contents, while the illitization was marked by an increase in the Fe and K contents of I-S.

As for the water-medium experiment, and to account for the mineral-composition changes in the I-S and carbonates, mean and extreme chemical compositions obtained from microprobe mappings after alteration were used to investigate the different equilibria (Figures 9, 11). For the carbonates, two possible reactions were possible (12 and 13):

$$0.1786\text{Dol} + 0.8214CO_2 + 0.7250\ \text{Anh} + 0.0918\text{Fe-Chl} = \text{Cc-}CO_2 + 0.1836H_2O + 0.3625\text{Py} + 0.0918\text{Qtz} + 0.0958\text{Kln} + 1.2688O_2 \quad (12)$$

$$\text{Cc-}CO_2 + 1.3329O_2 + 0.0974\text{Kln} + 0.0974\text{Qtz} + 0.3808\text{Py} + 0.1947H_2O = 0.1323\text{Dol-}CO_2 + 0.09737\text{Fe-Chl} + 0.7316\text{Anh} + 0.8677CO_2 \quad (13)$$

where $-CO_2$ indicates a CO_2-alteration experiment.

The two reactions cannot occur simultaneously but are sequential. The first reaction only involves primary dolomite and CO_2 to produce secondary calcite. This reaction is marked by a consumption of anhydrite and is limited by the second reaction which uses the O_2 produced in the first reaction to oxidize the pyrite. From these results, secondary calcite may only be an intermediate reaction, leading to the final precipitation of the secondary dolomite. If one assumes that all the CO_2 produced in the first reaction is consumed by the second one, CO_2 and anhydrite are produced during this reaction path. The role of the trivalent Fe in chlorite has been investigated and does not change the preceding observations.

With respect to the clays, one reaction exists and involves the secondary carbonates:

$$1.2391\text{clays} + 0.0187CO_2 + 0.0003\text{Cal-}CO_2 + 0.0054\text{Fe-Chl} + 0.0093\text{Py} + 0.2146H_2O = 0.4746\text{Qtz} + 0.0187\text{Anh} + 0.2377\text{Kln} + 0.0190\text{Dol-}CO_2 + \text{clays-}CO_2 \quad (14)$$

The valence of the Fe in chlorites only changes slightly the stoichiometric coefficients of reaction 14, in which some anhydrite and dolomite should be produced from pyrite and calcite, respectively, and a large amount of quartz and kaolinite is produced.

CONCLUSIONS

The mineralogical evolutions observed in all experimental mixtures are similar, except for the newly formed clays and carbonates that have different chemical compositions, depending on the CO_2/H_2O ratio of the medium.

From the analyses of possible reactions and equilibria involving primary and secondary minerals in the water- and CO_2-experiments, a coherent reaction path for each of them was constructed. In both experiments, the production of carbonates and secondary clays were in good agreement with the detailed experimental results. The reaction path of the water-experiment, however, leads to the precipitation of a significant amount of kaolinite, which is not observed in the experimental results. The XRD patterns show Fe-chlorite and kaolinite which are difficult to quantify together and may explain that discrepancy. In the CO_2-experiment, the reaction sequence leads to the consumption of some of the anhydrite before reprecipitation, and the precipitation of kaolinite. The mineralogical map resulting from microprobe mapping confirms that anhydrite is partially dissolved between the core and the rim, and precipitates at the rim.

Kaszuba *et al.* (2003) carried out the same type of experiment on a synthetic mix of quartz, orthoclase, microcline, and biotite to represent an aquifer, and the Silurian Maplewood Shale as an aquitard. Those authors concluded that the reactivity of the shales had to be included in studies aimed at sequestering CO_2. The amount of amorphous or crystallized Si in Kaszuba's study was probably related to the large amount of quartz, compared to the present study, in which only a slight increase in quartz content and no evidence of amorphous silica precipitation were observed.

The implications of the reactivity of shales for the integrity of the cap-rock are significant, including

https://doi.org/10.1346/CCMN.2009.0570509 Published online by Cambridge University Press

porosity changes and their consequences for permeability and fracturing processes. In particular, the porosity can be increased by an illitization of I-S minerals which is classically accompanied by a decrease in volume of particles, water expulsion, and precipitation of quartz. The hydraulic permeability can then be changed by this simple evolution of porosity, probably linked to textural evolutions. This can lead to water overpressures and some eventual fracture initiations. On the other hand, capillary pressures can decrease if the angle of contact between CO_2, or CO_2-enriched brines, and newly produced clay minerals increases. In this case, the consequence might simply be a leak of CO_2. Finally, the illitization of the smectite part of the clayey material can modify the mechanical response of the cap-rock and induce a decrease in plasticity. The textural transformation of the I-S particles can then change the permeability anisotropy and permit its increase in the lateral outlet.

Carbonate formations associated with clay compositional evolutions are a key factor in identifying and understanding the behavior of mineral reactivity. They clearly reacted first and initiated the reactivity of clays. In particular, the determination of the link between the carbonates and the clay reactivities is of major interest. The importance of these relationships will be investigated in a later study which will explore the reactivity of the cap-rock by use of numerical modeling. The study will also challenge the ability of a numerical model to reproduce quantitatively and qualitatively the present experimental reaction paths.

ACKNOWLEDGMENTS

This study was financed by the European PICOREF project. The authors acknowledge the support of C. Rigollet of Gaz de France and C. Pozo, M. Jullien, and J. Raynal for the use of the TEM at the Commissariat à l'Energie Atomique. The authors are also grateful for fruitful discussions with colleagues on the reactivity of clays. The constructive comments of the reviewers are also acknowledged.

REFERENCES

Al Darouich, T., Behar, F., and Largeau, C. (2006) Thermal cracking of the light aromatic fraction of Safaniya crude oil – experimental study and compositional modelling of molecular classes. *Organic Geochemistry*, **37**, 1130–1154.

Andre, L., Audigane, P., Azaroual, M., and Menjoz, A. (2007) Numerical modeling of fluid-rock chemical interactions at the supercritical CO_2-liquid interface during CO_2 injection into a carbonate reservoir, the Dogger aquifer (Paris Basin, France). *Energy Conversion and Management*, **48**, 1782–1797.

Béhar, F., Vandenbroucke, M., Tang, Y., Marquis, F., and Espitalié, J. (1997) Thermal cracking of kerogen in open and closed systems: determination of kinetics parameters and stoichiometric coefficients for oil and gas generation. *Organic Geochemistry*, **26**, 321–339.

Bonijoly, D., Hanot, F., Robellin, C., Serrano, O., Brosse, E., Houel, P., Naville, C., Rigollet, C., Manai, T., and Renoux, P. (2006) Site selection for CO_2 storage in deep aquifers of the Paris basin, France. *Proceedings of the International Symposium on Site Characterization for CO_2 Geologic Storage (CO_2SC)*, 2006, Berkeley, California, USA, pp. 69–70.

Brosse, E., de Smedt, G., Bonijoly, D., Garcia, D., Saysset, S., Manai, T., Thoraval, A., and Crepin, S. (2006) PICOREF: Towards an experimental site for CO_2 geological storage in the Paris Basin? Proceedings of the 8th International conference on Greenhouse Gas Control Technologies, 2006, Trondheim, Norway, p. 21.

Claret, F. (2001) Caractérisation structurale des transitions minéralogiques dans les formations argileuses: Contrôles et implications géochimiques des processus d'illitisation. Cas particulier d'une perturbation alcaline dans le Callovo-Oxfordien Laboratoire Meuse/Haute Marne. PhD thesis, Université Joseph Fourier-Grenoble I, Grenoble, France, 160 pp.

De Andrade, V., Vidal, O., Lewin, E., O'Brien, P., and Agaard, P. (2006) Quantification of electron microprobe compositional maps of rock thin sections: an optimized method and examples. *Journal of Metamorphic Geology*, **24**, 655–668.

Ergun, S. (1970) Xr-ray scattering by very defective lattices. *Physical Review B*, **131**, 3371–3380.

Gaus, I., Azaroual, M., and Czernichowski-Lauriol, I. (2005) Reactive transport modelling of the impact of CO_2 injection on the clayey cap rock at Sleipner (North Sea). *Chemical Geology*, **217**, 319–337.

Kaszuba, J.P., Janecky, D.R., and Snow, M.G. (2003) Carbon dioxide reaction processes in a model brine aquifer at 200 degrees C and 200 bars: implications for geologic sequestration of carbon. *Applied Geochemistry*, **18**, 1065–1080.

Kaszuba, J.P., Janecky, D.R., and Snow, M.G. (2005) Experimental evaluation of mixed fluid reactions between supercritical carbon dioxide and NaCl brine: Relevance to the integrity of a geologic carbon repository. *Chemical Geology*, **217**, 277–293.

Kretz, R. (1983) Symbols for rock-forming minerals. *American Mineralogist*, **68**, 277–279.

Lagneau, V., Pipart, A., and Catalette, H. (2005) Reactive transport modelling of CO_2 sequestration in deep saline aquifers. *Oil & Gas Science and Technology-Revue de l'Institut Francais du Petrole*, **60**, 231–247.

Lanson, B. and Besson, G. (1992) Characterization of the end of smectite-to-illite transformation: decomposition of X-ray patterns. *Clays and Clay Minerals*, **40**, 40–52.

Meunier, A. and Velde, B. (1989) Solid solutions in I-S mixed-layer minerals and illite. *American Mineralogist*, **74**, 1106–1112.

Meunier, A. and Velde, B. (2004) *Illite*. Springer-Verlag, Berlin, Heidelberg, 286 pp.

Parra, T., Vidal, O., and Agard, P. (2002) A thermodynamic model for Fe-Mg dioctahedral K white micas using data from phase-equilibrium experiments and natural pelitic assemblages. *Contributions to Mineralogy and Petrology*, **143**, 706–732.

Parra, T., Vidal, O., and Theye, T. (2005) Experimental data on the Tschermak substitution in Fe-chlorite. *American Mineralogist*, **90**, 359–370.

Plançon, A. and Drits, V.A. (2000) Phase analysis of clays using an expert system and calculation programs for X-ray diffraction by two- and three-component mixed-layer minerals. *Clays and Clay Minerals*, **48**, 57–62.

Ransom, B.L. and Helgeson, H.C. (1987) Thermodynamic prediction of the relative stabilities of illite and smectite in diagenetic processes, *Geological Society of America, 1987 annual meeting and exposition*. Geological Society of America, 1987, Vol. **19**, Issue 7, 813 pp.

Regnault, O., Lagneau, V., Catalette, H., and Schneider, H. (2005) Experimental study of pure mineral phases/supercritical CO_2 reactivity. Implications for geological CO_2

sequestration. *Comptes Rendus Geoscience*, **337**, 1331–1339.

Schroeder, P.A. (1990) Far infrared, X-ray powder diffraction, and chemical investigation of potassium micas. *American Mineralogist*, **75**, 983–991.

Środoń, J, Drits, V.A., McCarty, D.K., Hsieh, J.C.C., and Eberl, D.D. (2001) Quantitative X-ray diffraction analysis of clay-bearing rocks from random preparations. *Clays and Clay Minerals*, **49**, 514–528.

Vantelon, D., Pelletier, M., Michot, L.J., Barres, O., and Thomas, F. (2001) Fe, Mg and Al distribution in the octahedral sheet of montmorillonites. An infrared study in the OH-bending region. *Clay Minerals*, **36**, 3, 369–379

Velde, B. (1985) *Clay Minerals: A Physico-chemical Explanation of their Occurrence*. Elsevier, Amsterdam, 426 pp.

Velde, B. and Vasseur, G. (1992) Estimation of the diagenetic smectite to illite transformation in time-temperature space. *American Mineralogist*, **77**, 967–976.

Verlaguet, A., Brunet, F., Goffe, B., and Murphy, W.M. (2006) Experimental study and modeling of fluid reaction paths in the quartz-kyanite +/- muscovite-water system at 0.7 GPa in the 350–550 degrees C range: Implications for Al selective transfer during metamorphism. *Geochimica et Cosmochimica Acta*, **70**, 1772–1788.

Vidal, O. (2001) A thermodynamic model for Fe-Mg aluminous chlorite using data from phase equilibrium experiments and natural pelitic assemblages in the 100 degrees to 600 degrees C, 1 to 25 kb range. *American Journal of Science*, **301**, 557–592.

Vidal, O. and Parra, T. (2000) Exhumation paths of high pressure metapelites obtained from local equilibria for chlorite-phengite assemblages. *Geological Journal*, **35**, 139–161.

Vidal, O., Parra, T., and Vieillard, P. (2005) Thermodynamic properties of the Tschermak solid solution in Fe-chlorite: Application to natural examples and possible role of oxidation. *American Mineralogist*, **90**, 347–358.

Whitney, G. and Northrop, H.R. (1988) Experimental investigation of the smectite to illite reaction: Dual reaction mechanisms and oxygen-isotope systematics. *American Mineralogist*, **73**, 77–90.

(*Received 14 March 2008; revised 20 April 2009; Ms. 0140; A.E. J.W. Stucki*)